Advanced Plasmonic Photoconductive Sources for Pulsed and Continuous-Wave Terahertz Generation

by

Shang-Hua Yang

A dissertation submitted in partial fulfillment
of the requirements for the degree of
Doctor of Philosophy
(Electrical Engineering)
in the University of Michigan
2016

Doctoral Committee:

Associate Professor Mona Jarrahi, Co-Chair
Professor Herbert Winful, Co-Chair
Professor Almantas Galvanauskas
Associate Professor Vanessa Sih

2016

ACKNOWLEDGEMENTS

First and foremost, I would like to thank my advisor, Professor Mona Jarrahi, for giving me the opportunity and freedom to conduct this novel research. Because of her insightful guidance and patient instructions, I became an independent researcher and decided to devote my life to academia after my long journey in the States. I owe many thanks to Professor Peichen Yu and Dr. Jui-Nung Liu for their precious comments and suggestions during my undergraduate and graduate life. Moreover, I would like to thank and single out Dr. Christopher Berry, who is the first and most influential graduated student in our group. These research results would not have been possible without his contributions and assistance in so many ways. Also, he has been the best coffee mate during my time at the University of Michigan. I am indebted to Nezih Tolga Yardımcı for his full support, insightful input and precious comments on my research throughout these years. I thank all the people who have helped me reach this point: Professor Mehmet Ünlü, Dr. Mohammed Reza Hashemi, Dr. Semih Cakmakyapan, Dr. Ning Wang, Deniz Turan, Xiao Li and Amr Alaa Eldin. Lastly, I would like to express my deepest gratitude to my parents and my wife for their love and support, to let me chase my dream in the States. I would also like to thank all my friends in Ann Arbor and Los Angeles for their company during these years. I thank them all from the bottom of my heart.

TABLE OF CONTENTS

LIST OF FIGURES

LIST OF TABLES

ABSTRACT

Terahertz technology has attracted extensive attention because of its unique applications in environmental monitoring, space explorations, chemical identification, material characterization, security screening, medical imaging, and biological sensing. In the meantime, the practical feasibility of many terahertz systems is still limited by the low power, low efficiency, and bulky nature of existing terahertz sources. Among various techniques for terahertz generation, photoconduction has demonstrated very promising performance for generating both pulsed and continuous-wave (CW) terahertz radiation. Compared to other optically driven terahertz emitters based on nonlinear optical processes, performance of photoconductive terahertz emitters is not constrained by the Manley–Rowe limit and, therefore, can offer significantly higher optical-to-terahertz conversion efficiencies. In spite of their great promise, the performance of existing photoconductive terahertz emitters is severely limited by poor quantum efficiency of ultrafast photoconductors. This limitation is mainly caused by inefficient collection of the majority of the photocarriers in a sub-picosecond time scale.

To address this limitation, we introduce novel photoconductive terahertz source designs that incorporate plasmonic contact electrodes to offer significantly higher efficiencies compared to conventional designs. By utilizing plasmonic contact electrodes, a large

portion of the incident optical pump beam is concentrated and absorbed in close proximity to the plasmonic contact electrodes. Therefore, the average transport path length of photo-generated carriers to the contact electrodes is greatly reduced. As a result, higher photocurrent levels are fed to the terahertz antenna within the oscillation cycle of the terahertz radiation and higher optical-to-terahertz conversion efficiencies are achieved.

This dissertation covers the theoretical analysis and experimental results of high-performance narrowband/broadband plasmonic photoconductive terahertz sources. By utilizing plasmonic contact electrodes, we demonstrate record-high optical-to-terahertz conversion efficiencies as high as 7.5%, exhibiting three orders of magnitude higher efficiencies compared to conventional designs. We also demonstrate CW terahertz generation with a radiation frequency tuning range of more than 2 THz and a radiation power of 17 μW at 1 THz, exhibiting a 3-fold higher radiation power level compared to the state-of-the art. We also characterize spectral properties of the CW terahertz radiation from the demonstrated photoconductive terahertz source. Our analysis indicates that the spectral properties of the generated terahertz radiation are directly determined by the linewidth of the beating optical pump sources. This indicates the importance of the spectral characteristics of optical pump sources in achieving high-performance CW terahertz radiation sources for high spectral resolution, high accuracy, broadband terahertz spectroscopy systems and high-data-rate wireless communication systems. In the last part of this dissertation, we demonstrate an integrated photoconductive terahertz source with compact optical pump sources, which offers a very promising solution for future high-performance and compact terahertz imaging and sensing systems.

CHAPTER I

Introduction

1.1. Overview

Terahertz technology has attracted significant attention over the last decade with an increasing number of potential applications including biomedical imaging, security screening, high speed wireless communication, material identification, and space exploration. Compact, efficient and cost effective terahertz sources that can operate at room temperature are highly in demand to ensure that the applications mentioned above can be fully exploited. In addition to these general attributes, specific applications such as spectroscopy require narrow linewidth terahertz signals which can be readily tuned.

Current terahertz generation technologies can be divided into electronic and optical techniques. In the electronic category, electronic up-converters through frequency multiplication [1] and terahertz oscillators based on impact ionization avalanche transit-time (IMPATT) diodes, Gunn diodes, and resonance tunneling

diodes (RTDs) [2] have offered very promising compact terahertz sources. However, this category of sources has limitations in efficiency and frequency tunability. As an example, Schottky multipliers are a commercial solution that can generate terahertz signals approaching 3 THz with narrow linewidths and reasonable power levels (> 100 μW at 1 THz) [3]. However, they are limited in frequency tunability and their efficiency and linewidth/phase noise degrade as their multiplication order increases. Moreover, RTD based terahertz oscillators have demonstrated terahertz generation above 1 THz [4], but with limited frequency tunability and poor radiation linewidth/phase noise. In the optical category, terahertz quantum cascade lasers (QCLs) have shown great promise for direct generation of terahertz signals with very high signal power levels approaching 200 mW in continuous wave (CW) operation [5, 6]. However, they seldom operate below 2 THz (the minimum demonstrated frequency is 0.8 THz, achieved by applying external magnetic fields) and require significant cryogenic cooling. In addition, in order to achieve narrow linewidths below 1 MHz, complicated phase-locked loop (PLL) systems are required and limited tunability can only be obtained by mechanical means. Terahertz QCLs based on intracavity difference frequency generation have also shown great promise for room-temperature terahertz wave generation, but with limited frequency tunability and poor efficiency due to the utilized nonlinear process [7]. Another optical technique for terahertz generation is optical down-conversion. As an example, terahertz signal can be generated through difference frequency generation by nonlinear

mixing of two optical beams with a terahertz frequency difference [8]. This category of sources typically provides lower powers than other solutions but can offer continuous tunability over a broad terahertz frequency range through a compact and potentially integrated platform operating at room temperature. In addition, by use of optical comb based sources with phase correlated optical frequency lines difference frequency generation with photomixers can generate terahertz signals with long term stability and ultra-narrow linewidths (< 1 kHz) [9, 10].

1.2. Photoconductive Terahertz Sources

Among various techniques for terahertz generation, photoconduction has demonstrated very promising performance for generating both pulsed and continuous-wave (CW) terahertz radiation. This is mainly due to availability of high performance and compact optical lasers, enabling relatively high terahertz radiation powers at room temperature through a portable device platform. A photoconductive terahertz emitter is composed of an ultrafast photoconductor connected to a terahertz antenna and driven by an external optical pump. For narrowband/broadband terahertz radiation generation a heterodyned/pulsed optical pump beam is incident on the ultrafast photoconductor, generating photocarriers in the active region of the photoconductor. When a bias voltage is applied to the photoconductor, the bias electric field drifts the photocarriers to the

photoconductor contact electrodes, inducing a photocurrent that feeds the terahertz antenna and generates terahertz radiation. Compared to other optically driven terahertz emitters based on nonlinear optical processes, performance of photoconductive terahertz emitters is not constrained by the Manley–Rowe limit and, therefore, can offer significantly higher optical-to-terahertz conversion efficiencies. In spite of their great promise, the performance of existing photoconductive terahertz emitters is severely limited by poor quantum efficiency of ultrafast photoconductors. This limitation is mainly caused by inefficient collection of the majority of the photocarriers in a sub-picosecond time scale.

1.3. Dissertation Overview

Chapter II describes high-performance broadband photoconductive terahertz sources based on plasmonic contact electrodes. The experimental results also appeared in the *IEEE Transactions on Terahertz Science and Technology* [12] and *Optics Letters* [11].

Chapter III describes a comprehensive analysis and experimental demonstration of high-performance continuous-wave terahertz sources based on plasmonic contact electrodes. Sections of this chapter also appeared in the *Journal of Infrared, Millimeter and Terahertz Waves* [13] and *Applied Physics Letters* [14].

Chapter IV describes characterization of spectral properties of the terahertz radiation from plasmonic photomixers and their dependence on spectral properties

of the utilized optical pump beam. This detailed analysis also appeared in *Optics Express* [15].

Chapter V describes an integrated terahertz source composed of a bimodal laser diode and a plasmonic photomixer. This detailed analysis also appeared in *Optics Express* [16].

Chapter VI concludes the dissertation, emphasizing the specific contributions described in the dissertation.

References

[1] J. V. Siles and J. Grajal, "Physics-based design and optimization of schottky diode frequency multipliers for terahertz applications", *IEEE Transactions on Microwave Theory and Techniques*, vol. 58, pp. 1933–1942, 2010.

[2] M. Feiginov, C. Sydlo, O. Cojocari, and P. Meissner, "Resonant-tunneling-diode oscillators operating at frequencies above 1.1 THz", *Applied Physics Letters*, vol. 99, pp. 233506, 2011.

[3] http://vadiodes.com/

[4] S. Suzuki, M. Asada, A. Teranishi, H. Sugiyama, and H. Yokoyama, "Fundamental oscillation of resonant tunneling diodes above 1 THz at room temperature", *Applied Physics Letters*, vol. 97, pp. 242102, 2010.

[5] R. Köhler, A. Tredicucci, F. Beltram, H. E. Beere, E. H. Linfield, A. G. Davies, D. A. Ritchie, R. C. Iotti, and F. Rossi, "Terahertz semiconductor-heterostructure laser", *Nature,* vol. 417, pp. 156–159, 2002.

[6] B. S. Williams, "Terahertz quantum-cascade lasers", *Nature Photonics*, vol. 1, pp. 517–525, 2007.

[7] M. A. Belkin, F. Capasso, F. Xie, A. Belyanin, M. Fischer, A. Wittmann, and J. J. Faist, "Room temperature terahertz quantum cascade laser source based on

intracavity difference-frequency generation", *Applied Physics Letters*, vol. 92, pp. 201101, 2008.

[8] S. Preu, G. H. Dohler, S. Malzer, L. J. Wang, and A. C. Gossard, "Tunable, continuous-wave terahertz photomixer sources and applications", *Journal of Applied Physics*, vol. 109, pp. 061301, 2011.

[9] P. Acedo, H. Lamela, S. Garidel, C. Roda, J. P. Vilcot, G. Carpintero, I. H. White, K. A. Williams, M. Thompson, W. Li, M. Pessa, M. Dumitrescu, and S. Hansmann, "Spectral characterization of monolithic mode locked lasers for mm-wave generation and signal processing", *Electronics Letters*, vol. 42, pp. 928–929, 2006.

[10] H. Shams, T. Shao, M. J. Fice, P. M. Anandarajah, C. C. Renaud, F. Van Dijk, L. P. Barry, and A. J. Seeds, "100 Gb/s multicarrier THz wireless transmission system with high frequency stability based on a gain-switched laser comb source", *IEEE Photonics Journal*, vol. 7, pp. 1–11, 2015.

[11] S.-H. Yang and M. Jarrahi, "Enhanced light-matter interaction at nanoscale by utilizing high aspect-ratio metallic gratings", *Optics Letters*, vol. 38, pp. 3677, 2013.

[12] S.-H. Yang, M. R. Hashemi, C. W. Berry, M. Jarrahi, "7.5% Optical-to-Terahertz Conversion Efficiency Offered by Photoconductive Emitters with Three-Dimensional Plasmonic Contact Electrodes", *IEEE Transactions on Terahertz Science and Technology*, vol. 4, pp. 575–581, 2014.

[13] S.-H. Yang, R. Salas, Erica M. Krivoy, Hari P. Nair, S. R. Bank, M. Jarrahi, "Characterization of ErAs:GaAs and LuAs:GaAs Superlattice Structures for Continuous-Wave Terahertz Wave Generation through Plasmonic Photomixing", *Journal of Infrared, Millimeter and Terahertz Waves*, vol. 36, pp. 640–648, 2016.

[14] S.-H. Yang, M. Jarrahi, "Frequency-Tunable Continuous-Wave Terahertz Sources based on GaAs Plasmonic Photomixers", *Applied Physics Letters*, vol. 107, pp. 131111, 2015.

[15] S.-H. Yang, M. Jarrahi, "Spectral Characteristics of Terahertz Radiation from Plasmonic Photomixers", *Optics Express*, vol. 23, pp. 28522–28530, 2015.

[16] S.-H. Yang, R. Wans, X. Li, N. Wang, V. Cojocaru, J. O'Gorman, L. P. Barry, M. Jarrahi, "Tunable terahertz wave generation through a bimodal laser diode and plasmonic photomixer", *Optics Express*, vol. 23, pp. 31206–31215, 2015.

CHAPTER II

High-Performance Broadband Terahertz Sources

2.1. Overview

The performance of existing photoconductive terahertz emitters is severely limited by poor quantum efficiency of ultrafast photoconductors. This limitation is mainly caused by inefficient collection of the majority of the photocarriers in a sub-picosecond time scale. In order to efficiently contribute to terahertz radiation, the transit time of the photocarriers to the photoconductor contact electrodes should be within a fraction of the terahertz oscillation period. Considering the carrier transportation dynamics inside semiconductors, only the photocarriers which are generated within distances of 100 nm from the contact electrode can efficiently contribute to terahertz radiation, even under sufficient bias electric fields. However, since the minimum spot size of the optical pump beam is diffraction limited, the majority of the photocarriers cannot be generated within distances of

~100 nm from the contact electrodes and, therefore, cannot efficiently contribute to terahertz generation.

2.2. Enhanced Performance by Utilizing Plasmonic Nanostructures

Recent studies have shown that incorporating plasmonic contact electrodes in photoconductive terahertz emitters can significantly enhance the photoconductor quantum efficiency by concentrating a larger fraction of the incident pump photons within nanoscale distances from the contact electrodes [1–7]. This enhancement mechanism has been widely used in various photoconductive terahertz emitters with a variety of device architectures and in various operational settings, demonstrating significant optical-to-terahertz conversion efficiency enhancements as high as two-orders of magnitude [8,9]. To date, the existing photoconductive terahertz emitters that utilize plasmonic contact electrodes have all been based on two-dimensional plasmonic contact electrodes fabricated on the surface of the photo-absorbing semiconductor substrate. By use of two-dimensional plasmonic contact electrodes, the concentration of the photocarriers near the contact electrodes is enhanced for the photocarriers that are generated near the surface of the photo-absorbing semiconductor substrate. However, the optical-to-terahertz efficiency of the photoconductive emitter is still limited by the photocarriers generated deeper than ~100 nm in the photo-absorbing substrate. To address this limitation, we develop photoconductive terahertz emitters based on

three-dimensional plasmonic nanostructures embedded inside the photo-absorbing substrate.

2.3 Three-Dimensional Plasmonic Nanostructures

2.3.1 Light-Matter Interaction at Nanoscale

Extraordinary light transmission through nanoscale apertures [10–14] has enabled several unique functionalities and device capabilities including high-resolution optical spectroscopy and microscopy [15–19], nanolithography [20,21], high-capacity data storage [22], enhanced nonlinear phenomena [23], enhanced light emission and lasing [24–27], high-efficiency and high-speed photodetection [28,29], enhanced photoconductive terahertz radiation power [6–9], and enhanced photoconductive terahertz detection sensitivity [4]. However, further fulfillment of many of these unique functionalities requires extending the light–matter interaction lengths at the nanoscale, which is severely limited by nanofabrication challenges.

2.3.2 Design

Normally, light transmission through subwavelength metallic apertures is diffraction limited. However, utilizing a periodic subwavelength metallic grating mitigates this limitation by excitation of surface waves, which assist efficient coupling of a transverse magnetic (TM)-polarized incident light beam into the

transverse electromagnetic (TEM) guided modes of subwavelength slab waveguides formed by the metallic grating. Interaction of a TM-polarized optical beam with subwavelength metallic gratings has been analyzed extensively [30–35], indicating several guided modes at resonance wavelengths of the subwavelength slab waveguides formed by the subwavelength metallic gratings.

Figure 2.1(a) shows the high-aspect-ratio metallic grating we designed to enable efficient interaction of a TM-polarized optical beam in the 760–860 nm wavelength range with GaAs nanostructures integrated with the metallic grating over interaction lengths as long as two times of the effective optical wavelength in the GaAs nanostructures. For this purpose, the grating is designed to excite the fourth-order TEM guided mode of the subwavelength slab waveguides formed by the metallic grating for 380–440 nm grating height. Additionally, the thickness of the SiO_2 antireflection coating is set to maximize coupling of the 760–860 nm optical beam into the GaAs nanostructures. It should be noted that by extending the metallic grating height, higher-order TEM guided modes can be excited by the incident TM-polarized optical beam, further extending the light–matter interaction lengths at the nanoscale.

We used a finite-element solver (COMSOL) to analyze the interaction of the incident optical beam with the GaAs nanostructures integrated with the designed metallic grating. Figure 2.1(b) shows the transmission spectrum of a normally incident TM-polarized optical beam, into the GaAs nanostructures integrated with

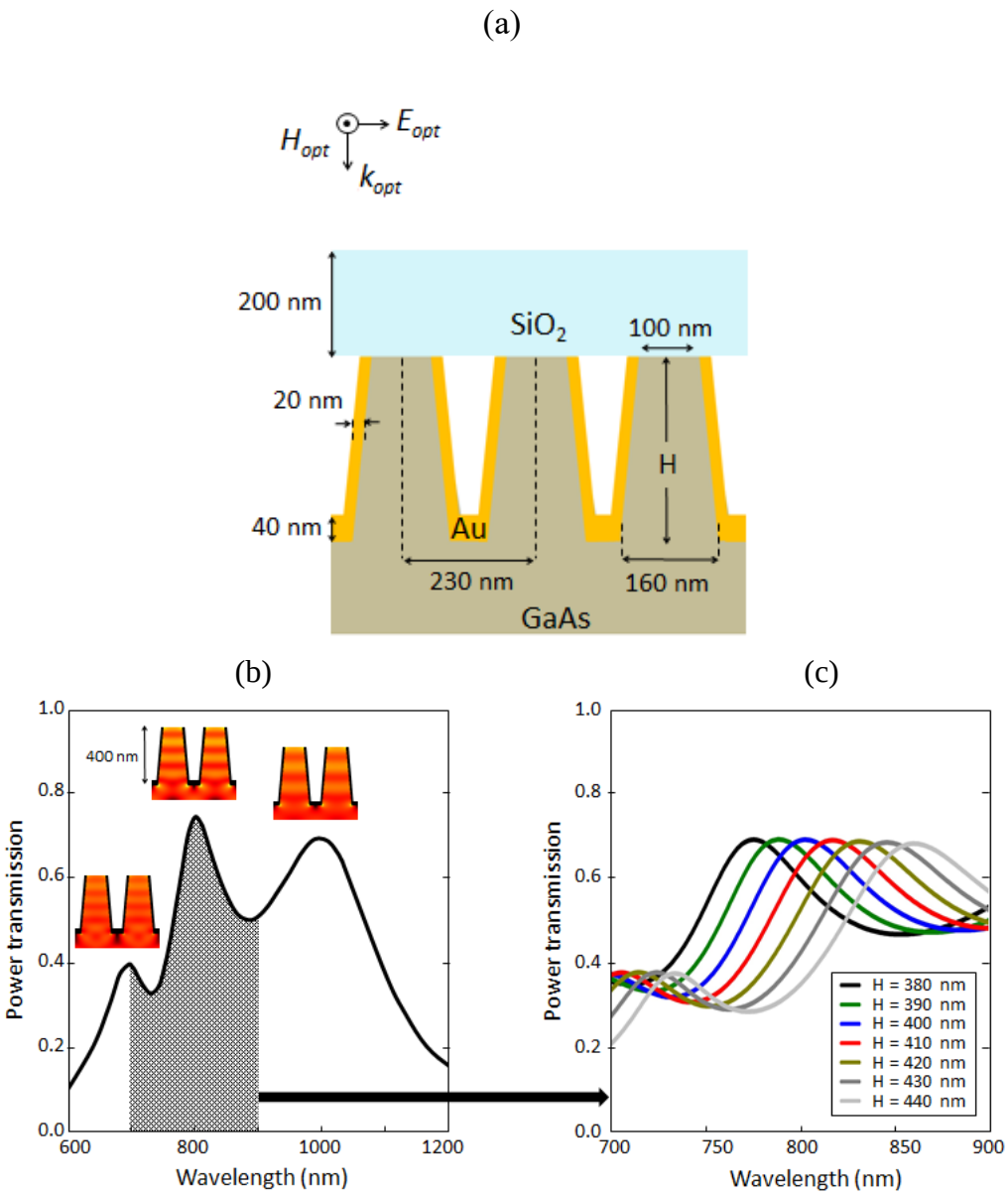

Figure 2.1 (a) Cross-sectional view of the designed high-aspect-ratio metallic grating integrated with GaAs nanostructures, which supports multiple TEM guided modes in response to a TM-polarized incident optical beam. The metal thickness should be larger than or comparable with the metal skin depth to confine light inside the subwavelength slab waveguide formed by the metallic gratings. Within this regime, light–matter interaction with the GaAs nanostructures would be independent of the metal thickness on the sidewalls. (b) Transmission spectrum of a normally incident TM-polarized optical beam, into the GaAs nanostructures integrated with the designed metallic grating for a grating height of 400 nm. Inset shows the electric field color map of the transmitted optical beam at the transmission peaks. (c) Transmission spectrum of the normally incident TM-polarized optical beam into the GaAs nanostructures integrated with the designed metallic grating as a function of the grating height.

the designed metallic grating for a grating height of 400 nm. The transmission spectrum in the 600–1200 nm optical wavelength range indicates transmission peaks at 1000, 800, and 700 nm, which correspond to the third-, fourth-, and fifth-order TEM guided modes of the subwavelength slab waveguides formed by the metallic grating. Excitation of the third-, fourth-, and fifth-order TEM guided modes can be also observed from the electric field color map of the transmitted optical beam at the transmission peaks [Fig. 2.1 (b) inset]. The relatively higher transmission of the fourth-order TEM guided mode is due to use of a 200 nm thick SiO_2 antireflection coating optimized for the 760–860 nm optical wavelength range. Figure 2.1(c) shows the transmission spectrum of the normally incident TM-polarized optical beam into the GaAs nanostructures integrated with the designed metallic grating as a function of the grating height. By changing the grating height in the 380–440 nm range, the optical transmission peak (the fourth-order TEM guided mode of the subwavelength slab waveguides formed by the metallic gratings) varies in the 760–860 nm wavelength range.

2.3.3 Fabrication

Prototypes of the designed high-aspect-ratio metallic grating were fabricated on a semi-insulating GaAs substrate. The fabrication process started with depositing a 200 nm thick SiO_2 film by plasma-enhanced chemical vapor deposition on the GaAs substrate [Fig. 2.2(a)], followed by patterning nanoscale Ni gratings with

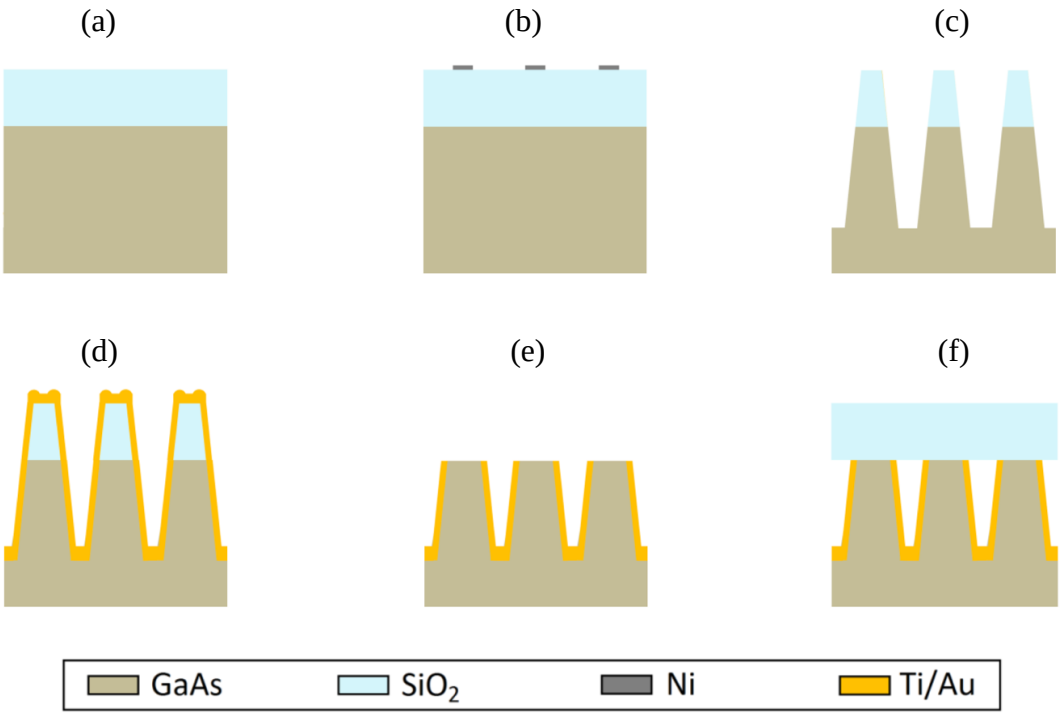

Figure 2.2 Fabrication process of the high-aspect-ratio nanoscale metallic gratings: (a) deposition of a SiO_2 layer, (b) pattering a Ni hard mask, (c) etching the SiO_2 layer and the underlying GaAs substrate, (d) Ti/Au sputtering, (e) lift-off, and (f) deposition of a SiO_2 antireflection coating.

electron beam lithography to form a hard mask for etching nanoscale GaAs regions [Fig. 2.2(b)]. The SiO_2 film and the underlying GaAs substrate were etched afterward using an inductively coupled plasma reactive ion etching technique (ICP-RIE) to form high-aspect-ratio nanograting structures [Fig. 2.2(c)]. Metallic gratings were then formed by sputtering Ti/Au [Fig. 2.2(d)], followed by liftoff [Fig. 2.2(e)]. In order to have a uniform metal coverage on the sidewalls of the GaAs nanostructures, the slope of the GaAs sidewalls was specifically controlled by adjusting the ICP-RIE parameters. A SiO_2 antireflection coating was deposited to cover the top of the GaAs nanostructures [Fig. 2.2(f)]. Finally, contact

pads were deposited and connected to the metallic grating regions. In order to observe the impact of the grating height on the optical interaction with the designed high-aspect-ratio metallic grating, two grating prototypes with grating heights of 400 and 440 nm were fabricated and characterized under the same experimental conditions.

2.3.4 Experiment Results

The scanning electron microscope (SEM) image of a fabricated grating with a 400 nm grating height is shown in Fig. 2.3(a). In order to characterize the optical wave interaction with the GaAs nanostructures defined by the fabricated metallic gratings, a TM-polarized optical beam from a Ti:sapphire laser was focused onto each grating, and the induced photocurrent was measured over 700– 860 nm optical wavelength range. The optical transmission spectrum into the GaAs nanostructures integrated with the grating prototypes was calculated from the measured photocurrent spectrum.

Figures 2.3(b) and 2.3(c) show the optical transmission spectrum through the grating prototypes with grating heights of 400 and 440 nm, respectively. The results indicate two transmission peaks in the 700–860 nm wavelength range for the fabricated high-aspect-ratio grating prototypes. As predicted by our theoretical model, the observed transmission peaks are associated with the fourth- and fifth-order TEM guided modes of the subwavelength slab waveguides formed by the

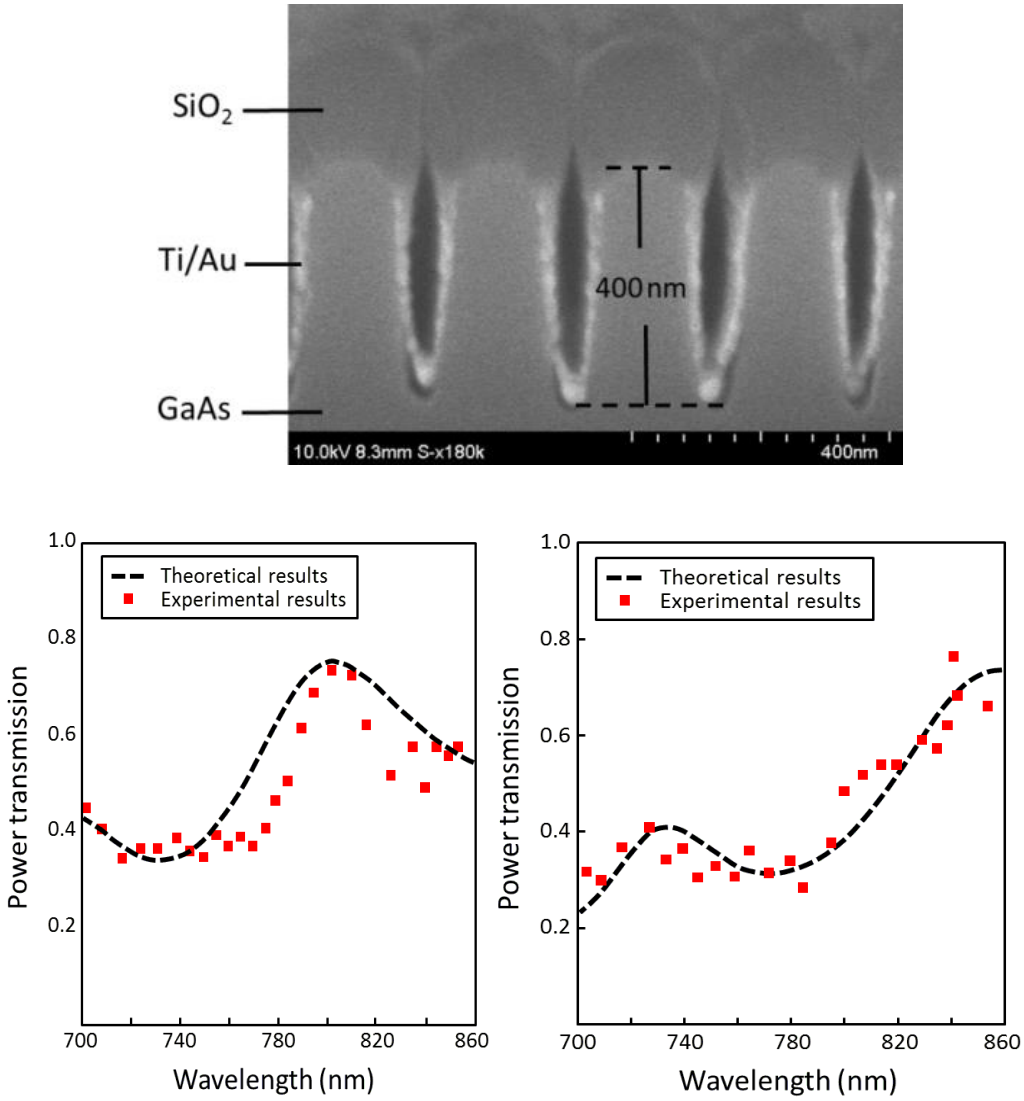

Figure 2.3 (a) SEM image of an implemented high-aspect-ratio grating with a 400 nm grating height. The optical transmission spectrum into the GaAs nanostructures integrated with the grating prototypes is shown in (b) and (c) for grating heights of 400 and 440 nm, respectively.

metallic grating. This can be further confirmed by the dependence of the observed transmission peaks on the grating height. As the grating height is extended from 400 to 440 nm, the transmission peak associated with the fourth-order TEM

guided mode is shifted from 800 to 860 nm, and the transmission peak associated with the fifth-order TEM guided mode is shifted from 700 to 730 nm. The relatively higher transmission coefficient of the fourth-order guided modes is due to the use of a 200 nm thick SiO_2 antireflection coating optimized for the 760–860 nm optical wavelength range, enabling efficient interaction of more than 70% of the incident optical beam with GaAs nanostructures over interaction lengths as long as two times of the effective optical wavelength inside GaAs nanostructures.

2.4 Plasmonic Photoconductive Terahertz Sources based on 3D Plasmonic Contact Electrodes

In order to demonstrate the significant optical-to-terahertz conversion efficiency enhancement through use of three-dimensional plasmonic contact electrodes, a photoconductive terahertz emitter with three-dimensional plasmonic contact electrodes is implemented, and its performance is compared with a similar photoconductive emitter with two-dimensional plasmonic contact electrodes.

2.4.1 Design

2.4.1.1 Design of Photoconductive Terahertz Emitter

Fig. 2.4 shows the schematic diagram of the plasmonic photoconductive terahertz emitters fabricated on the same low temperature grown (LT) GaAs substrate with

a carrier lifetime of ~400 fs. Both plasmonic photoconductive emitters utilize the same logarithmic spiral terahertz antenna, well-suited for pulsed terahertz generation. The logarithmic spiral antenna is designed to offer a broadband radiation resistance of 70–100 Ω while maintaining a reactance value near 0 Ω over the 0.1–2 THz frequency range [36–38]. The plasmonic photoconductive emitters are mounted on identical hyper-hemispherical silicon lenses, used for collecting and collimating the generated terahertz radiation from the back-side of the LT–GaAs substrate. The plasmonic contact electrodes of both photoconductive emitters cover a 15 × 15 μm^2 area for the cathode and anode contacts. The end-to-end spacing between the anode and cathode plasmonic contact electrodes is 5 μm. The geometry and spacing of the anode and cathode contacts are selected to provide high bias electric field levels for the entire device active area such that the photocarriers within ~100 nm from the contact electrodes travel at the saturation velocity of ~10^7 cm/s.

2.4.1.2 Design of the Two-Dimensional Plasmonic Electrodes

The plasmonic photoconductive emitter with two-dimensional plasmonic contact electrodes on the surface of the LT–GaAs substrate [Fig. 2.4(a)] incorporates Au gratings with 200 nm pitch, 100 nm spacing, 50 nm height, and a 150 nm thick SiO_2 anti-reflection coating. This design allows excitation of surface plasmon waves along the Au gratings and transmission of 70% of the optical pump power

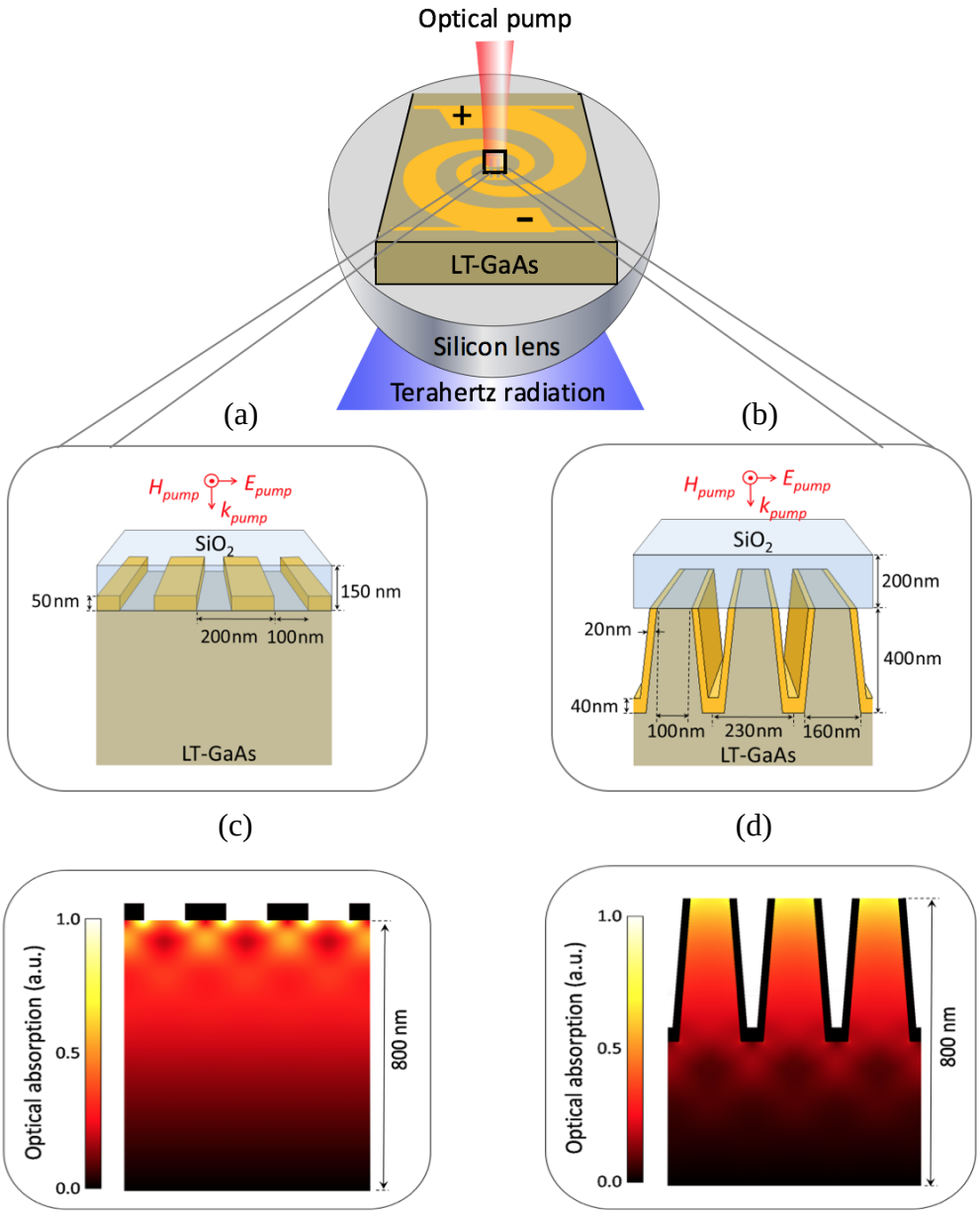

Figure 2.4 Schematic diagram of plasmonic photoconductive emitters with: (a) two-dimensional plasmonic contact electrodes on the surface of the LT–GaAs substrate and (b) three-dimensional plasmonic contact electrodes embedded inside the LT–GaAs substrate. Color plot of optical absorption in the LT–GaAs substrate in response to a TM-polarized optical beam at 800 nm wavelength incident on the (c) two-dimensional and (d) three-dimensional plasmonic contact electrodes, respectively.

into the substrate in response to a transverse magnetic (TM)-polarized optical pump at 800 nm wavelength [35]. When a TM-polarized incident optical pump at

800 nm wavelength is incident on the two-dimensional plasmonic contact electrodes, the bias electric field separates the cluster of the photo-generated electrons and holes and drifts them toward the anode and cathode contact electrodes, respectively. The induced photocurrent is then fed to the logarithmic spiral antenna, generating terahertz radiation. The use of the two-dimensional plasmonic contact electrodes on the surface of the LT–GaAs substrate significantly enhances the concentration of the photocarriers near the photoconductor contact electrodes, enhancing the number of the photocarriers that are drifted to the contact electrodes in a sub-picosecond time-scale to efficiently contribute to terahertz radiation. However, since the plasmonic contact electrodes are located on the surface of the substrate, a large fraction of the photocarriers generated within depths beyond ~100 nm from the surface of the substrate cannot be drifted to the contact electrodes within a sub-picosecond time-scale to efficiently contribute to terahertz radiation. Use of three-dimensional plasmonic contact electrodes embedded inside the LT–GaAs substrate mitigates this limitation by significantly increasing the concentration of the majority of the photocarriers in close proximity to the contact electrodes.

2.4.1.3 Design of the Three-Dimensional Plasmonic Electrodes

The plasmonic photoconductive emitter with three-dimensional plasmonic contact electrodes embedded inside the substrate [Fig. 2.4(b)] incorporates high-aspect

ratio metallic gratings that cover the sidewalls of nanoscale LT–GaAs device active regions sandwiched between the metallic gratings. Utilizing a periodic arrangement of nanoscale metallic gratings allows excitation of surface plasmon waves along the gratings, which enables efficient coupling of a TM-polarized incident optical wave into the TEM guided modes of subwavelength slab waveguides formed by the metallic gratings [30,32,39,40]. The height of the LT–GaAs nanostructures determines the excited modes inside the subwavelength slab waveguides formed by the metallic gratings. Therefore, by extending the metallic grating height, higher order TEM guided modes can be excited by the incident optical beam. For our presented three-dimensional plasmonic contact electrodes [Fig. 3.4(b)], the high-aspect ratio metallic gratings are designed to excite the fourth-order TEM guided mode of the subwavelength slab waveguides formed by the metallic gratings in response to a TM-polarized optical pump at 800 nm wavelength. To reduce the Fresnel reflection losses a 200 nm SiO_2 anti-reflection coating layer is used on the top of the LT–GaAs nanostructures. This design allows efficient coupling of 70% of the 800 nm optical pump into the LT–GaAs nanostructures with 400 nm height [39].

We have used a multi-physics finite-element solver (COMSOL) to compare the optical absorption profile in the LT–GaAs substrate near the two-dimensional plasmonic contact electrodes [see Fig. 2.4(c)] and three-dimensional plasmonic contact electrodes [Fig. 2.4(d)]. The results indicate that a significantly larger

fraction of photocarriers are generated within ~100 nm distance from the three-dimensional plasmonic contact electrodes. Consequently, the number of the photocarriers drifted to the three-dimensional plasmonic contact electrodes within a sub-picosecond time-scale is significantly higher than that of the two-dimensional plasmonic contact electrodes, resulting in considerably higher quantum efficiencies.

2.4.2 Fabrication

We have fabricated prototypes of the presented plasmonic photoconductive emitters based on the two-dimensional and three-dimensional plasmonic contact electrodes on a LT–GaAs substrate with a substrate resistivity of $10^7\ \Omega \cdot$ s. and electron hall mobility of 200 $cm^2/V{\cdot}s$. For the photoconductive emitter with two-dimensional plasmonic contact electrodes, the fabrication process starts with patterning the plasmonic contact electrodes using electron-beam lithography, followed by deposition of Ti/Au (50/450 Å) and liftoff. Next, the 150 nm thick SiO_2 anti-reflection coating is deposited using plasma enhanced chemical vapor deposition. Contact vias are then opened by etching the SiO_2 coating. Finally, the bias lines and antennas are patterned using optical lithography followed by Ti/Au (10/400 nm) deposition and liftoff [39].

For the photoconductive emitter with three-dimensional plasmonic contact electrodes, the fabrication process starts with deposition of a 200 nm thick SiO_2

film by plasma enhanced chemical vapor deposition. Next, nanoscale Ni gratings, which serve as a hard mask for etching the underlying SiO_2 layer, are patterned on the surface of the SiO_2 film using electron beam lithography followed by Ni deposition and liftoff. By using inductively coupled plasma reactive ion etching (ICP-RIE), nanoscale SiO_2 gratings with 200 nm height are then formed to serve as a hard mask for shaping the high-aspect ratio LT–GaAs nanostructures. Metallic gratings are then formed by sputtering Ti/Au (2/20 nm) on the sidewalls of the LT–GaAs nanostructures. In order to maintain high-uniformity metal coverage on the sidewalls of the LT–GaAs nanostructures, the slope of the SiO_2 and LT–GaAs sidewalls are specifically controlled by adjusting the ICP-RIE etch parameters. The SiO_2 hard mask is then removed by a wet etching process. A 200 nm thick SiO_2 anti-reflection coating is then deposited to cover the top of the LT–GaAs nanostructures. Finally, the logarithmic spiral terahertz antennas and bias lines are formed using optical lithography followed by Ti/Au (20/400 nm) deposition and liftoff [39]. Fig. 2.5 shows the optical microscope and scanning electron microscope (SEM) images of the fabricated plasmonic photoconductive emitter incorporating three-dimensional plasmonic contact electrodes. The cross-sectional SEM image of the high-aspect ratio metallic gratings shows the configuration of the LT–GaAs nanostructures and the complete metallic coverage on the sidewalls of the LT–GaAs nanostructures.

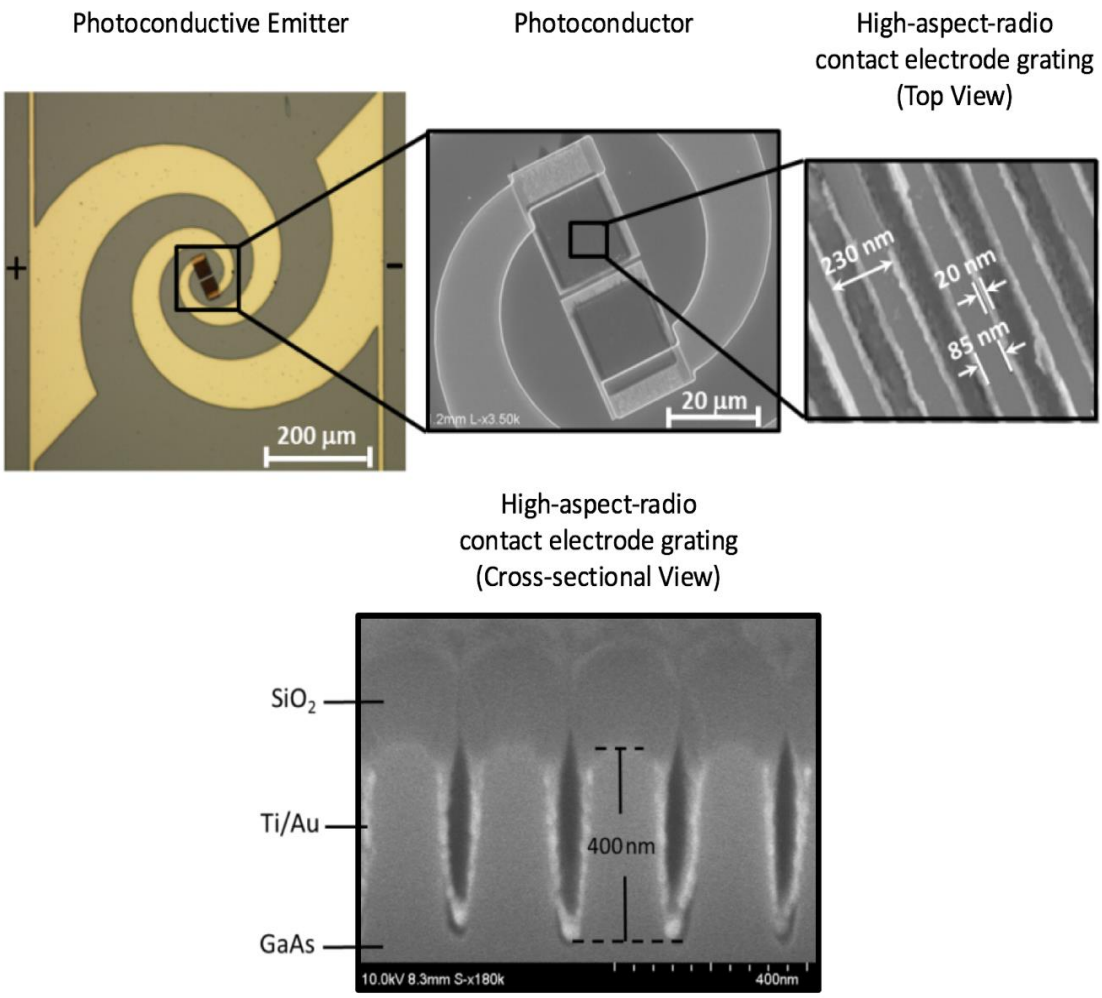

Figure 2.5 Microscope image of the photoconductive emitter based on three-dimensional plasmonic contact electrodes and SEM images of the three-dimensional plasmonic contact electrodes based on high-aspect-ratio metallic gratings.

2.4.3 Experimental Setup

The fabricated devices are then mounted and centered on a high resistivity hyper-hemispherical silicon lens. In order to characterize the terahertz radiation performance of the photoconductive terahertz emitter prototypes based on two-dimensional and three-dimensional plasmonic contact electrodes, a TM-polarized

optical beam from a Ti:sapphire mode-locked laser with a pulse width of 200 fs and wavelength of 800 nm is used to pump the photoconductive emitters. The optical pump, with a 5 μm FWHM circular spot size, is asymmetrically focused on the anode plasmonic contact electrodes to maximize the induced ultrafast photocurrent feeding the terahertz antenna and to offer the optimum impedance loading to the antenna [41,42].

2.4.3 Experimental Results

The photocurrent characteristics of the photoconductors based on the two-dimensional and three-dimensional plasmonic contact electrodes are shown in Fig. 2.6(a) and 2.6(b), respectively. At the same optical pump power and bias voltage, the induced ultrafast photocurrent in the photoconductor with three-dimensional plasmonic contact electrodes is significantly higher than the induced ultrafast photocurrent in the photoconductor with two-dimensional plasmonic contact electrode. This verifies the predicted quantum-efficiency enhancement as the result of using the three-dimensional plasmonic contact electrodes, which accumulates a significantly larger number of photocarriers in close proximity to the contact electrodes. By accumulating larger number of photocarriers in ~100 nm distances from the contact electrodes, a larger number of the photocarriers can travel to the contact electrodes before recombination in the LT–GaAs substrate.

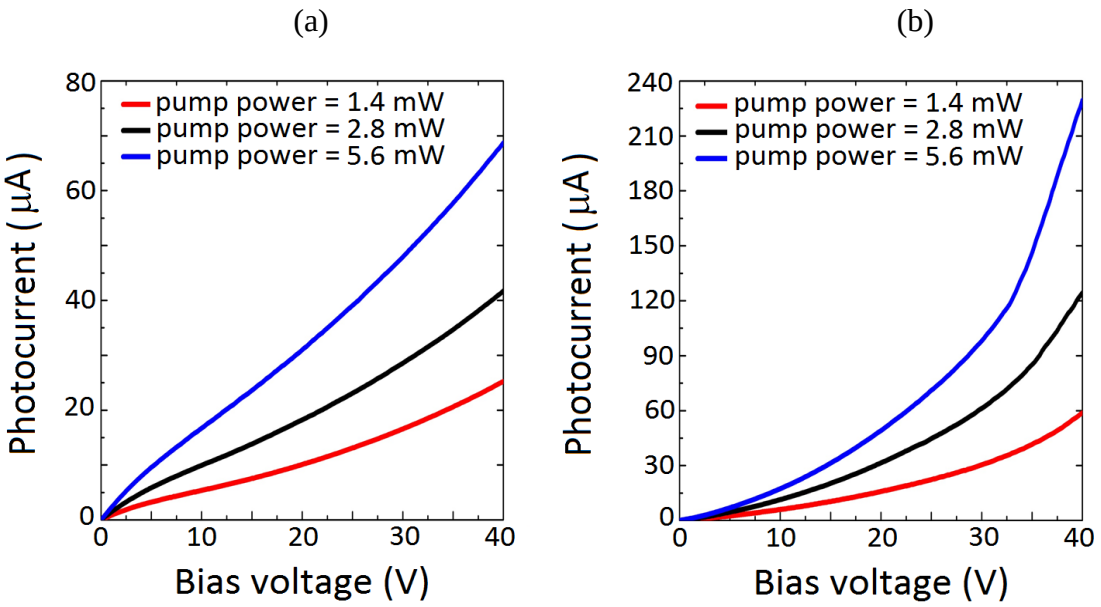

Figure 2.6 Output photocurrent of the photoconductors based on (a) two-dimensional plasmonic contact electrodes and (b) three-dimensional plasmonic contact electrodes as a function of the bias voltage and optical pump power.

A pyroelectric detector (Spectrum Detector, Inc, SPI-A-65 THz) is used to measure the radiated power from the plasmonic photoconductive terahertz emitters. Fig. 2.7(a) and 2.7(b) shows the radiated power from the photoconductive emitters with the two-dimensional and three-dimensional plasmonic contact electrodes, respectively. Terahertz radiation powers up to 105 μW are measured from the photoconductive emitter with three-dimensional plasmonic contact electrodes at the optical pump power of 1.4 mW, exhibiting the record-high optical-to-terahertz power conversion efficiency of 7.5%. Moreover, the radiated terahertz power from the photoconductive emitter with three-dimensional plasmonic contact electrodes is an order of magnitude higher than the radiated terahertz power from the

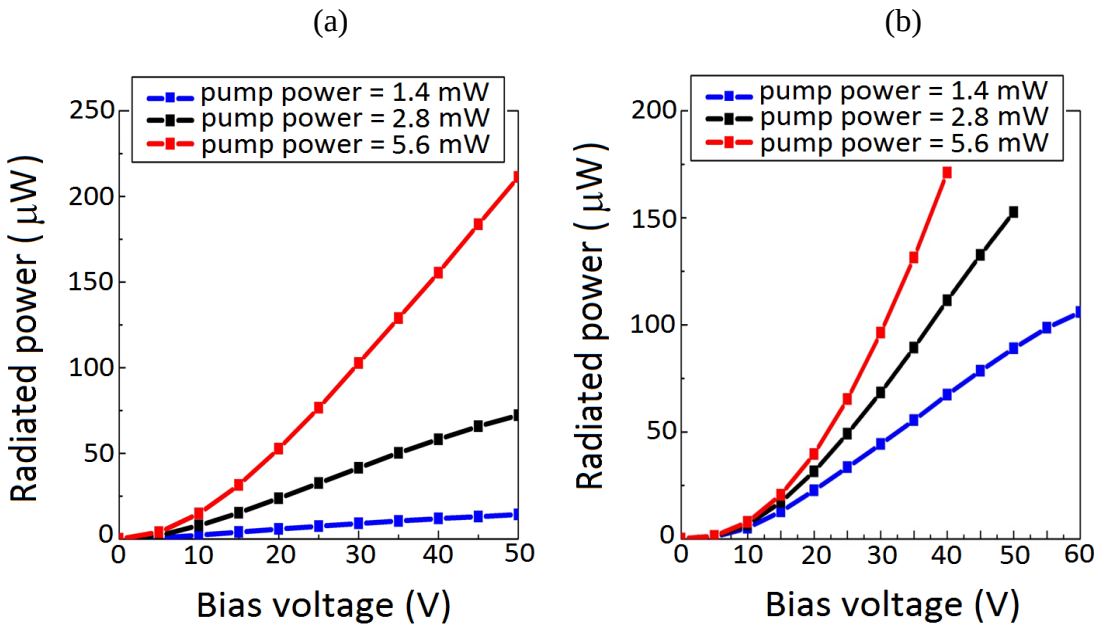

Figure 2.7 Radiated power from the photoconductive emitters based on (a) two-dimensional plasmonic contact electrodes and (b) three-dimensional plasmonic contact electrodes as a function of the bias voltage and optical pump power.

comparable photoconductive emitter with two-dimensional plasmonic contact electrodes at the optical pump power of 1.4 mW. The observed optical-to-terahertz conversion efficiency enhancement is due to the impact of the three-dimensional plasmonic contact electrodes embedded inside the LT–GaAs substrate, enhancing the photoconductor quantum-efficiency by accumulating the majority of the photocarriers in close proximity to the contact electrodes.

While the output power of the plasmonic photoconductive emitters increase as a function of the optical pump power, their optical-to-terahertz conversion efficiency is slightly degraded at higher optical pump powers (Fig. 2.8). This is due to the carrier screening effect [43], decreasing the bias electric field when a large number of electro-hole pairs are separated from each other. It should be

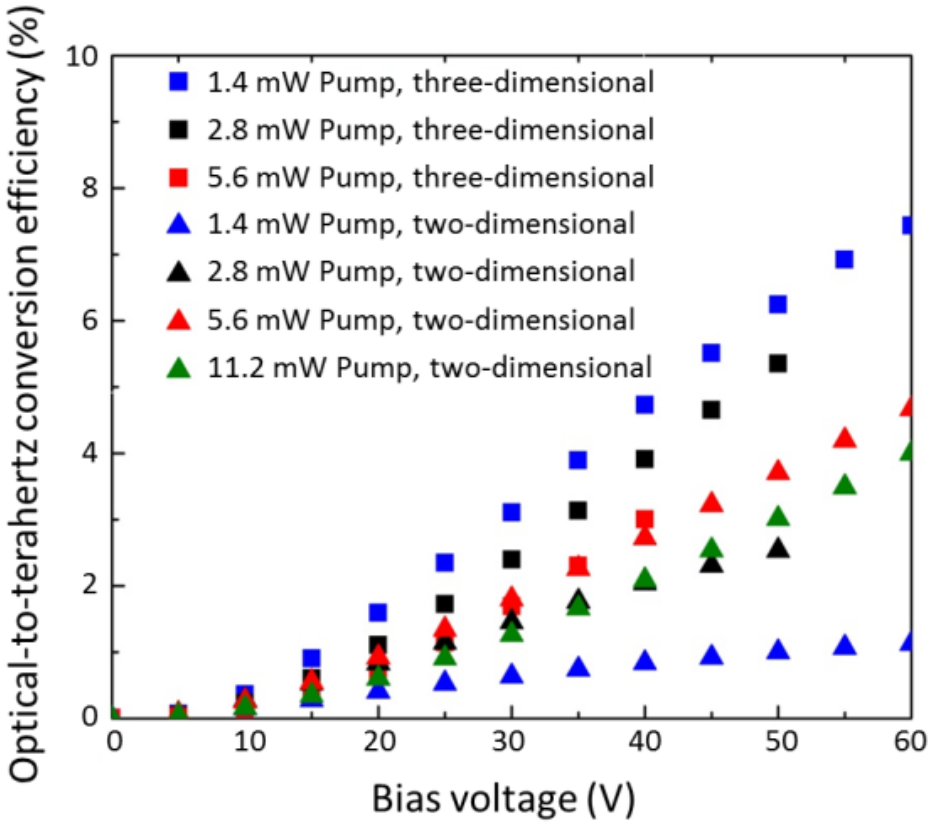

Figure 2.8 Optical-to-terahertz conversion efficiency of the photoconductive emitters based on the two-dimensional and three-dimensional plasmonic contact electrodes as a function of the optical pump power and bias voltage.

noted that the optical-to-terahertz conversion efficiency degradation at higher optical pump powers is more pronounced for the photoconductive emitter based on the three-dimensional plasmonic contact electrodes. This is because a larger number of photocarriers are localized in close proximity to the contact electrodes in the design with three-dimensional plasmonic contact electrodes. Therefore, separating a larger number of electron-hole pairs in the three-dimensional design induces a larger electric field in the opposite direction to the bias electric field.

(a)

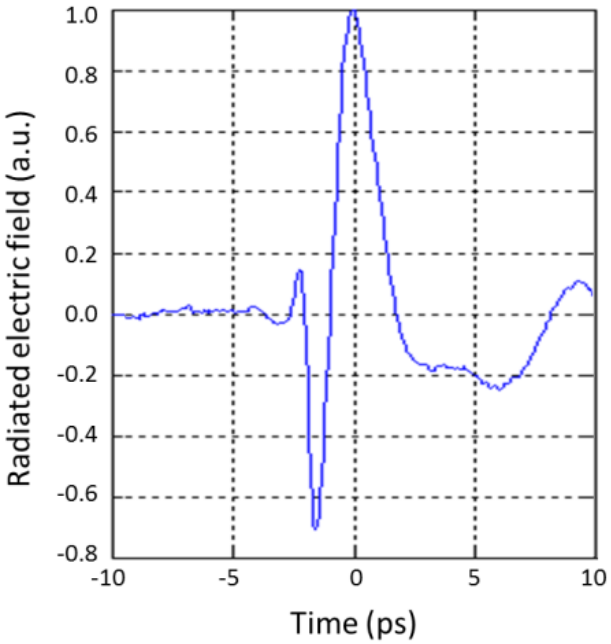

(b)

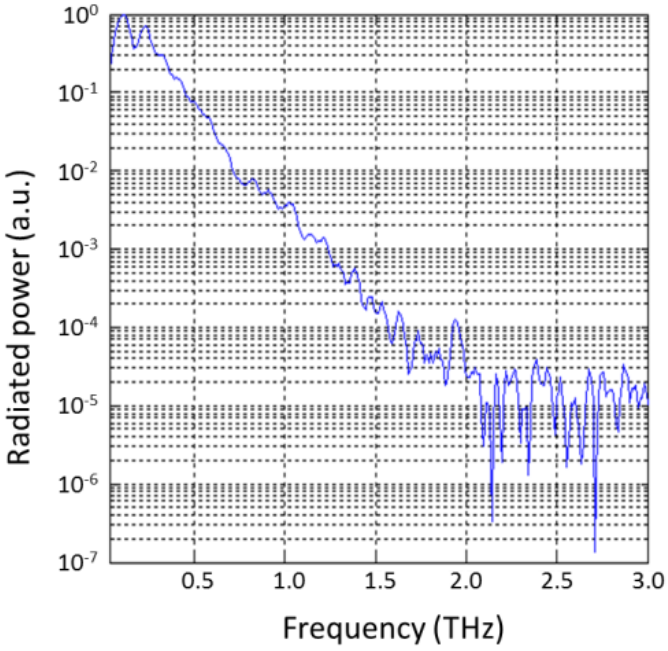

Figure 2.9 Measured radiated electric field in the (a) time-domain and (b) radiated power in frequency-domain for the plasmonic photoconductive emitter with the three-dimensional plasmonic contact electrodes.

Finally, the radiated field from the plasmonic photoconductive emitters is characterized in a time-domain terahertz spectroscopy setup with electro-optic detection in a 1 mm thick ZnTe crystal [40]. Fig. 2.9(a) and 2.9(b) shows the time-domain radiated field and frequency-domain radiated power from the photoconductive emitter with three-dimensional plasmonic contact electrodes, indicating a radiation bandwidth of more than 2 THz. It should be mentioned that the measured time-domain and frequency-domain radiation properties are identical for both photoconductive emitters based on two-dimensional and three-dimensional plasmonic contact electrodes in the 0.1–3 THz frequency range. This is because of the fact that the radiated spectrum is mainly affected by the spectral properties of the terahertz antenna, which is identical for both photoconductive emitters.

2.4.4 Discussion

In summary, a novel plasmonic photoconductive terahertz emitter based on three-dimensional plasmonic contact electrodes integrated with a logarithmic spiral antenna on a LT–GaAs substrate is presented. The three-dimensional plasmonic contact electrodes are based on high-aspect-ratio metallic gratings embedded inside the LT–GaAs substrate. The use of the three-dimensional plasmonic contact electrodes manipulates the spatial distribution of the photocarriers in the substrate and enhances the number of the photocarriers in close proximity to the contact

electrodes. Therefore, efficient transport of the majority of the photocarriers to the contact electrodes in a sub-picosecond time-scale in achieved, mitigating the tradeoff between high quantum-efficiency and ultrafast operation and offering high optical-to-terahertz conversion efficiencies. In order to evaluate the performance of the photoconductive emitter with three-dimensional plasmonic contact electrodes, a comprehensive characterization of the device performance in comparison with a similar photoconductive emitter with two-dimensional plasmonic contact electrodes is presented. By use of the three-dimensional plasmonic contact electrodes, we experimentally demonstrate a record-high optical-to-terahertz conversion efficiency of 7.5% at an optical pump power of 1.4 mW. This optical-to-terahertz conversion efficiency is an order of magnitude higher than the optical-to-terahertz conversion efficiency offered by the two-dimensional plasmonic contact electrodes. The unprecedented power efficiency enhancement offered by the three-dimensional plasmonic contact electrodes can be further extended to offer higher optical-to-terahertz conversion efficiencies through use of higher aspect ratio three-dimensional contact electrodes and use of larger device active areas to mitigate the carrier screening effect [44–46].

References

[1] S.-G. Park, K. H. Jin, M. Yi, J. C. Ye, J. Ahn, and K.-H. Jeong, “Enhancement of terahertz pulse emission by optical nanoantenna”, *ACS Nano,* vol.6, pp. 2026, 2012.

[2] S. Liu, X. Shou, and A. Nahata, “Coherent detection of multiband terahertz radiation using a surface plasmon-polariton based photoconductive antenna”, *IEEE Transactions on Terahertz Science and Technology*, vol. 1, pp. 412–415, 2011.

[3] S.-G. Park, Y. Choi, Y.-J. Oh, and K.-H. Jeong, “Terahertz photoconductive antenna with metal nanoislands”, *Optics Express*, vol. 20, p. 25530, 2012.

[4] N. Wang, M. R. Hashemi, and M. Jarrahi, “Plasmonic photoconductive detectors for enhanced terahertz detection sensitivity”, *Optics Express,* vol. 21, pp. 17221, 2013.

[5] B. Heshmat, H. Pahlevaninezhad, Y. Pang, M. Masnadi-Shirazi, R. B. Lewis, T. Tiedje, R. Gordon, and T. E. Darcie, “Nanoplasmonic terahertz photoconductive switch on GaAs”, *Nano Letters*, vol. 12, pp. 6255–6259, 2012.

[6] C. W. Berry and M. Jarrahi, “Plasmonically-enhanced localization of light into photoconductive antennas”, in *Conference on Lasers and Electro-Optics*, 2010, pp. CFI2, Optical Society of America.

[7] C. W. Berry and M. Jarrahi, “Ultrafast photoconductors based on plasmonic gratings”, in 2011 *International Conference on Infrared, Millimeter, and Terahertz Waves*. Oct. 2011, pp. 1–2, IEEE.

[8] C. W. Berry and M. Jarrahi, “Terahertz generation using plasmonic photoconductive gratings”, *New Journal of Physics*, vol. 14, pp. 105029, 2012.

[9] C. W. Berry, N. Wang, M. R. Hashemi, M. Unlu, M. Jarrahi, “Significant Performance Enhancement in Photoconductive Terahertz Optoelectronics by Incorporating Plasmonic Contact Electrodes”, *Nature Communications*, vol. 4, pp. 1622, 2013.

[10] C. Genet and T. W. Ebbesen, “Light in tiny holes”, *Nature*, vol. 445, 39–46, 2007.

[11] J. A. Schuller, E. S. Barnard, W. Cai, Young C. Jun, J. S. White and M. L. Brongersma, “Plasmonics for extreme light concentration and manipulation”, *Nature Materials*, vol. 9, pp. 193–204, 2010.

[12] W. L. Barnes, A. Dereux, and T. W. Ebbesen, “Surface plasmon subwavelength optics”, *Nature*, vol. 424, pp. 824–830, 2003.

[13] F. J. Garcia-Vidal, L. Martin-Moreno, T. W. Ebbesen, and L. Kuipers, “Light passing through subwavelength apertures”, *Reviews of Modern Physics*, vol. 82, pp. 729, 2010.

[14] H. Liu and P. Lalanne, “Microscopic theory of the extraordinary optical transmission”, *Nature*, vol. 452, pp. 728–731, 2008.

[15] E. Betzig and J. K. Trautman, “Near-field optics: microscopy, spectroscopy, and

surface modification beyond the diffraction limit", *Science*, vol. 257, pp. 189–194, 1992.

[16] J. V. Coe, J. M. Heer, S. Teeters-Kennedy, H. Tian, and K. R. Rodriguez, "Localized Surface Plasmon Resonance Spectroscopy and Sensing", *Annual Review of Physical Chemistry*, vol. 58, pp. 267–297, 2007.

[17] M. E. Stewart, C. R. Anderton, L. B. Thompson, J. Maria, S. K. Gray, J. A. Rogers, and R. G. Nuzzo, "Nanostructured Plasmonic Sensors", *Chemical Reviews*, vol. 108, pp. 494–521, 2008.

[18] R. Gordon, D. Sinton, K. L. Kavanagh and A. G. Brolo, "A New Generation of Sensors Based on Extraordinary Optical Transmission", *Accounts of Chemical Research*, vol. 41, pp. 1049–1057, 2008.

[19] B.-Y. Hsieh, N. Wang, and M. Jarrahi, "Toward Ultrafast Pump-Probe Measurements at the Nanoscale", *Optics and Photonics News*, vol. 22, pp. 48, 2011.

[20] W. Srituravanich, N. Fang, C. Sun, Q. Luo, and X. Zhang, "Plasmonic Nanolithography", *Nano Letters*, vol. 4, pp. 1085–1088, 2004.

[21] D. B. Shao and S. C. Che, "Surface-plasmon-assisted nanoscale photolithography by polarized light", *Applied Physics Letters*, vol. 86, pp. 253107, 2005.

[22] X. Shi and L. Hesselink, "Mechanisms for Enhancing Power Throughput from Planar Nano-Apertures for Near-Field Optical Data Storage", *Japanese Journal of Applied Physics*, vol. 41, Part 1, 1632, 2002.

[23] A. Nahata, R. A. Linke, T. Ishi, and K. Ohashi, "Enhanced nonlinear optical conversion from a periodically nanostructured metal film", *Optics Letters*, vol. 28, 423–425, 2003.

[24] J. Vuckovic, M. Loncar, and A. Scherer, "Plasmon enhanced optical near-field probing of metal nanoaperture surface emitting laser", *Optics Express*, vol. 12, pp. 6391–6396, 2004.

[25] J. Hashizume, F. Koyama, "Surface Plasmon Enhanced Light-Emitting Diode", *IEEE Journal of Quantum Electronics*, vol. 36, pp. 1131–1144, 2000.

[26] C. Liu, V. Kamaev, and Z. V. Vardeny, "Efficency enhancement of an organic lightemitting diode with a cathode forming two-dimensional periodic hole array", *Applied Physics Letters*, vol. 86, pp. 143501, 2005.

[27] A. Polman, "Plasmonics applied", *Science*, vol. 322, pp. 868, 2008.

[28] E. Ozbay, "Plasmonics: Merging Photonics and Electronics at Nanoscale Dimensions", *Science*, vol. 311, pp. 189, 2006.

[29] J. White, G. Veronis, Z. Yu, E. S. Barnard, A. Chandran, S. Fan and M. L. Brongersma, "Extraordinary optical absorption through subwavelength slits", *Optics Letters,* vol. 34, 686–688, 2009.

[30] P. B. Catrysse, G. Veronis, H. Shin, J. T. Shen, and S. Fan, "Guided modes supported by plasmonic films with a periodic arrangement of subwavelength slits", *Applied Physics Letters,* vol. 88, pp. 031101, 2006.

[31] J. T. Shen and P. M. Platzman, "Properties of a one-dimensional metallophotonic crystal", *Physical Review B,* vol. 70, pp. 035101, 2004.

[32] B.-Y. Hsieh and M. Jarrahi, "Analysis of periodic metallic nano-slits for efficient interaction of terahertz and optical waves at nano-scale dimensions", *Journal of Applied Physics*. vol. 109, pp. 084326, 2011.

[33] C. W. Berry, J. Moore, and M. Jarrahi, "Design of reconfigurable metallic slits for terahertz beam modulation", *Optics Express,* vol. 19, pp. 1236, 2011.

[34] Y. Takakura, "Optical resonance in a narrow slit in a thick metallic screen", *Physics Review Letters,* vol. 86, pp. 5601, 2001.

[35] S. Astilean, Ph. Lalanne, and M. Palamaru, "Light transmission through metallic channels much smaller than the wavelength*", Optics Communications,* vol. 175, pp. 265–273, 2000.

[36] Y. Huo, G. W. Taylor, and R. Bansal, "Planar log-periodic antennas on extended hemishperical silicon lenses for millimeter/submillimeter wave detection applications", *Journal of Infrared, Millimeter and Terahertz Waves*, vol. 23, pp. 819–839, 2002.

[37] E. R. Brown, A. W. M. Lee, B. S. Navi, and J. E. Bjarnason, "Characterization of a planar self-complementary square-spiral antenna in the THz region", *Microwave and Optical Technology Letters*, vol. 48, pp. 524–529, 2006.

[38] C. W. Berry, M. R. Hashemi, M. Jarrahi, "Generation of High Power Pulsed Terahertz Radiation using a Plasmonic Photoconductive Emitter Array with Logarithmic Spiral Antennas", *Applied Physics Letters,* vol. 104, pp. 081122, 2014.

[39] S.-H. Yang and M. Jarrahi, "Enhanced light-matter interaction at nanoscale by utilizing high aspect-ratio metallic gratings", *Optics Letters,* vol. 38, pp. 3677, 2013.

[40] C. W. Berry, M. R. Hashemi, M. Unlu, and M. Jarrahi, "Design, fabrication, and experimental characterization of plasmonic photoconductive terahertz emitters", *Journal of Visualized Experiments*, vol. 77, pp. E50517, 2013.

[41] S. E. Ralph and D. Grischkowsky, "Trap-enhanced electric fields in semi-insulators: The role of electrical and optical carrier injection", *Applied Physics*

Letters, vol. 59, pp. 1972–1974, 1991.

[42] P. C. Upadhya, W. Fan, A. Burnett, J. Cunningham, A. G. Davies, E. H. Linfield, J. Lloyd-Hughes, E. Castro-Camus, M. B. Johnston, and H. Beere, "Excitation-density-dependent generation of broadband terahertz radiation in an asymmetrically excited photoconductive antenna", Optics Letters, vol. 32, pp. 2297–2299, 2007.

[43] G. C. Loata, M. D. Thomson, T. Löffler, and H. G. Roskos, "Radiation field screening in photoconductive antennae studied via pulsed terahertz emission spectroscopy", *Applied Physics Letters*, vol. 91, pp. 232506, 2007.

[44] T. Hattori, K. Egawa, S. I. Ookuma, and T. Itatani, "Intense terahertz pulses from large-aperture antenna with interdigitated electrodes", *Japanese Journal of Applied Physics*, vol. 45, pp. L422–L424, 2006.

[45] H. Kim, A. Polley, and S. E. Ralph, "Efficient photoconductive terahertz source using line excitation", Optics Letters, vol. 30, pp. 2490–2492, 2005.

[46] A. Dreyhaupt, S. Winnerl, T. Dekorsy, and M. Helm, "High-intensity terahertz radiation from a microstructured large-area photoconductor", Applied Physics Letters, vol. 86, pp 121114, 2005.

CHAPTER III

High-Performance Continuous-Wave Terahertz Sources

3.1. Overview

Photomixing is one of the most commonly used techniques for generating continuous-wave (CW) terahertz radiation for a variety of imaging, sensing, and communication applications [1–3]. It can offer narrow spectral linewidths, high spectral purity, and wide frequency tunability at room temperature [4–12]. A conventional photomixer is composed of an ultrafast photoconductor integrated with a terahertz antenna pumped by two CW optical beams with a terahertz beating frequency. When the optical pump beam is incident on the ultrafast photoconductor, a photocurrent is induced at the terahertz beating frequency. The induced photocurrent drives the terahertz antenna to generate radiation at the terahertz beating frequency. Despite their great attributes, the scope and potential use of conventional photomixers are limited by the low efficiency of their ultrafast photoconductors, which limits their terahertz radiation power levels.

3.2. Plasmonic Photomixer

3.2.1 Method

To address this limitation, we introduce a novel photomixer design that incorporates plasmonic contact electrodes to offer significantly higher efficiencies compared to conventional photomixers. By utilizing plasmonic contact electrodes, a large portion of the incident optical pump beam is concentrated and absorbed in close proximity to the plasmonic contact electrodes [8–21]. Therefore, the average transport path length of photo-generated carriers to the contact electrodes is greatly reduced. As a result, higher photocurrent levels are fed to the terahertz antenna within the oscillation cycle of the terahertz radiation and higher optical-to-terahertz conversion efficiencies are achieved. We demonstrate a plasmonic photomixer fabricated on a low temperature (LT) grown GaAs substrate, which offers more than 2 THz radiation frequency tuning range and a record-high CW radiation power of 17 μW at 1 THz, exhibiting a 3-fold higher radiation power level compared to the state-of-the art.

3.2.2 Design

Prototypes of plasmonic photomixers are fabricated on a low temperature grown (LT) GaAs substrate with a substrate resistivity of 10^7 cm Ω and carrier lifetime of 400 fs (Fig. 3.1(a)). The designed plasmonic contact electrodes consist of metallic gratings with 200 nm pitch, 100 nm spacing, 5/45 nm Ti/Au height, and a

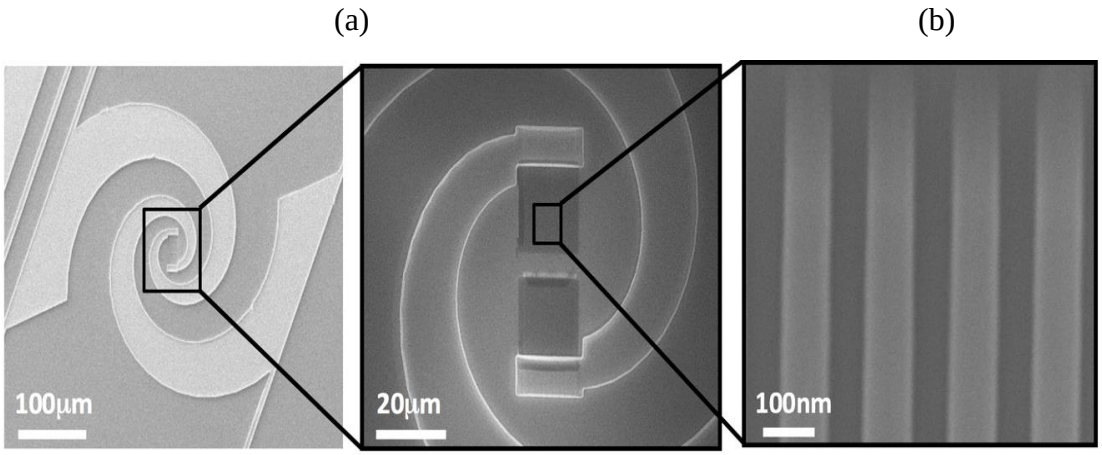

Figure 3.1 (a) Scanning electron microscope (SEM) images of a fabricated plasmonic photomixer comprised of a logarithmic spiral antenna integrated with plasmonic contact electrodes on a LT-GaAs substrate. (b) SEM image of the plasmonic contact electrodes.

150 nm thick SiO_2 anti-reflection coating (Fig. 3.1(b)). The geometry of the metallic gratings is optimized to offer 70% power transmission for a TM-polarized optical pump beam through the metallic gratings into the LT-GaAs substrate in the 780nm wavelength range. Each plasmonic contact electrode covers a 15 × 15 μm^2 area with a 5 μm end-to-end spacing between the anode and cathode contact electrodes. This enables maintaining a relatively uniform photocarrier drift velocity near the plasmonic contact electrodes across the entire plasmonic contact electrode area without reaching the breakdown electric field [15–16]. In order to sustain high radiation power levels over a wide frequency range, we use a logarithmic spiral antenna to offer a broadband radiation resistance of 70–100 Ω while maintaining a reactance value near 0 Ω over 0.1–2 THz frequency range [20].

3.2.3 Fabrication

The fabrication process starts with patterning the plasmonic contact electrodes using electron-beam lithography, followed by deposition of Ti/Au (5/45 nm) and liftoff. Bias lines and the logarithmic spiral antennas are patterned next by using optical lithography followed by Ti/Au (10/400 nm) deposition and liftoff. Next, the 150nm-thick SiO_2 anti-reflection coating layer is patterned by optical lithography and the SiO_2 layer is deposited by plasma enhanced chemical vapor deposition (PECVD). Finally, the plasmonic photo- mixers are mounted on a hyper hemispherical silicon lens used for collecting and collimating the radiated terahertz beam from the back-side of the LT-GaAs substrate.

3.2.4 Electrical and Optical Characterization

3.2.4.1 Experimental Setup

Figure 3.2 shows the experimental setup constructed to characterize the optical and terahertz radiation properties of the plasmonic photomixers. It consists of two fiber-coupled, wavelength-tunable, distributed-feedback (DFB) lasers with 783nm and 785nm center wavelengths (TOPTICA #LD-0783-0080-DFB-1 and #LD-0785-0080-DFB-1). Both pump lasers have a 2MHz spectral linewidth and 2.4nm wavelength tunability range. In order to optimize the optical- to-terahertz conversion efficiency, the optical beams from the two pump lasers are set to have the same power levels. The outputs of the two pump lasers are combined in a

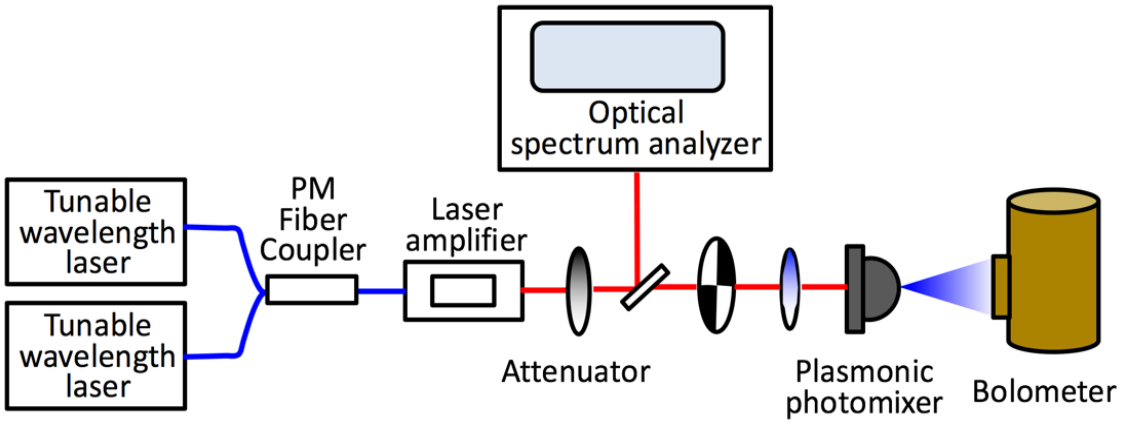

Figure 3.2 Experimental setup for characterizing the LT-GaAs plasmonic photomixers.

polarization-maintaining (PM) fiber coupler and amplified by a semiconductor optical amplifier (TOPTICA BOOSTA PRO 780). The amplified optical beam is collimated and asymmetrically focused onto the edge of the anode contact electrode.

This maximizes the terahertz radiation power by concentrating a large portion of the photo-generated electrons in close proximity to the anode contact electrode and facilitating their drift to the terahertz antenna within a terahertz oscillation period. The optical pump beam is simultaneously monitored by an optical spectrum analyzer by placing a pellicle along the beam path of the optical pump incident on the plasmonic photomixers. Finally, the generated terahertz beam is collimated and measured by using a calibrated silicon bolometer from Infrared Laboratories with a peak-to-peak responsivity of 2.83×10^5 V/W at 40 Hz.

3.2.4.2 Experimental Results

Figures 3.3(a) and 3.3(b) show the induced photocurrent and radiated terahertz power from a fabricated plasmonic photomixer at 1 THz frequency as a function of the optical pump power and bias voltage. At relatively low incident pump powers and low bias voltages, the measured photocurrent and terahertz power data points are well fitted to a quadratic curve (Fig. 3.4(a)). This is expected for photomixers under ideal conditions. However, when increasing the optical pump power, the radiated terahertz power levels deviate from the quadratic curve and lower terahertz powers are radiated (Fig. 3.4(a)) due to the carrier screening effect. This is because a larger amount of electron-hole pairs is generated and separated from each other, which induces an opposing electric field between the device contact electrodes. Higher bias voltages are required to overcome the opposing electric field induced by photocarrier separation. At a pump power of 350 mW, a record-high terahertz radiation power of 17 μW is obtained at 1 THz. Figure 3.4(b) shows a comparison between the radiated power from the plasmonic photomixer at 1 THz and previously demonstrated photomixers with broadband and resonant antennas [6–7, 22–32], indicating record-high terahertz radiation power offered by the presented LT-GaAs plasmonic photomixer. The radiated power from the presented plasmonic photomixer is even higher than the power levels offered by uni-traveling carrier (UTC) photomixers, despite their completely different substrate structure and operation principles. Therefore, utilizing plasmonic contact electrodes in UTC photomixers can offer even higher radiation power levels.

(a)

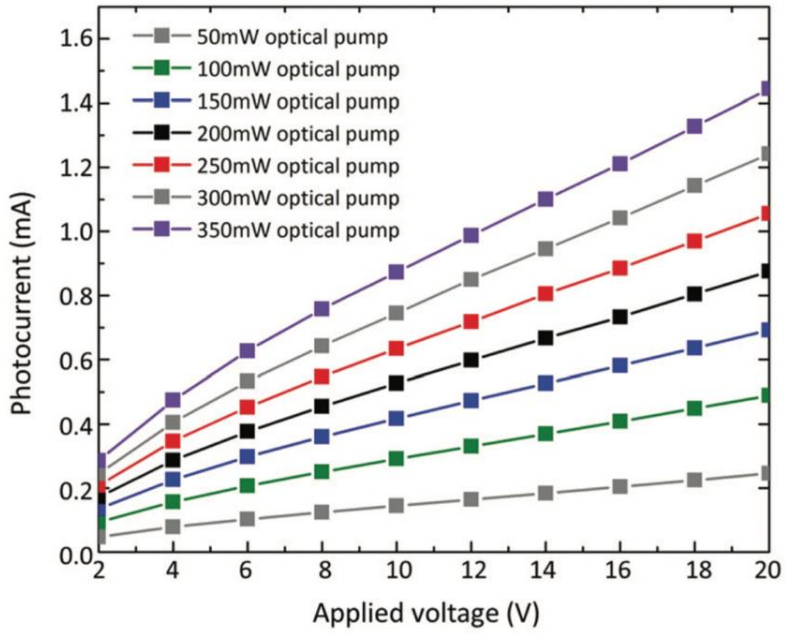

(b)

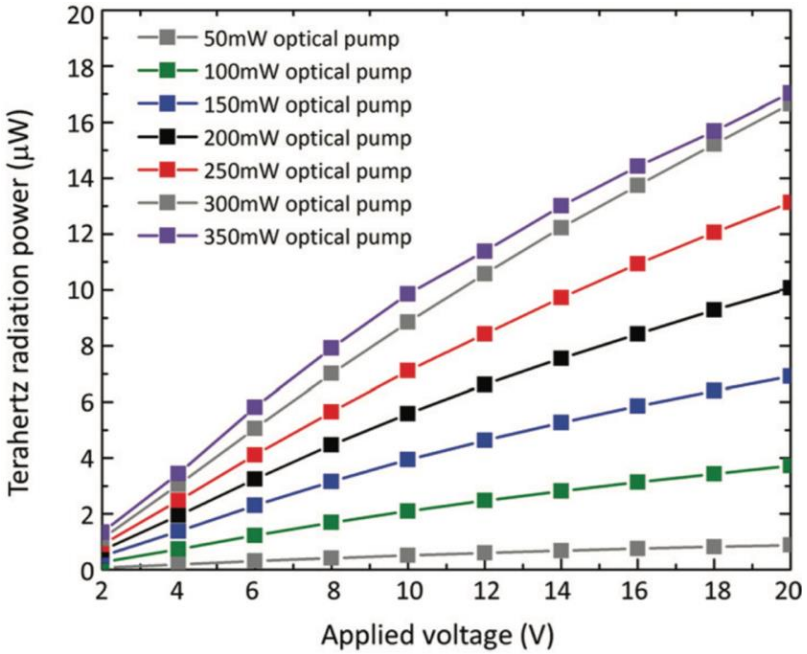

Figure 3.3 The induced photocurrent and radiated terahertz power of a fabricated LT-GaAs plasmonic photomixer at 1 THz as a function of the optical pump power and bias voltage are shown in (a) and (b), respectively.

(a)

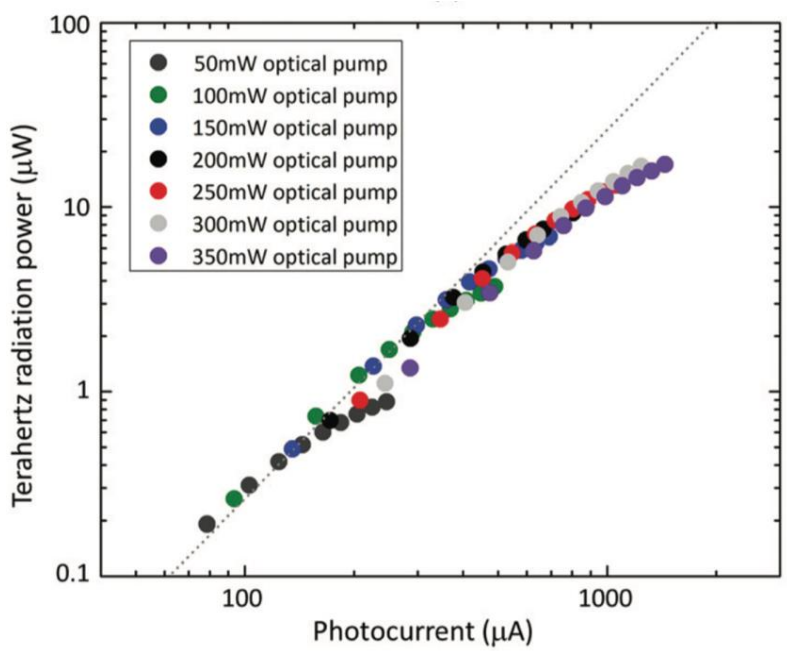

(b)

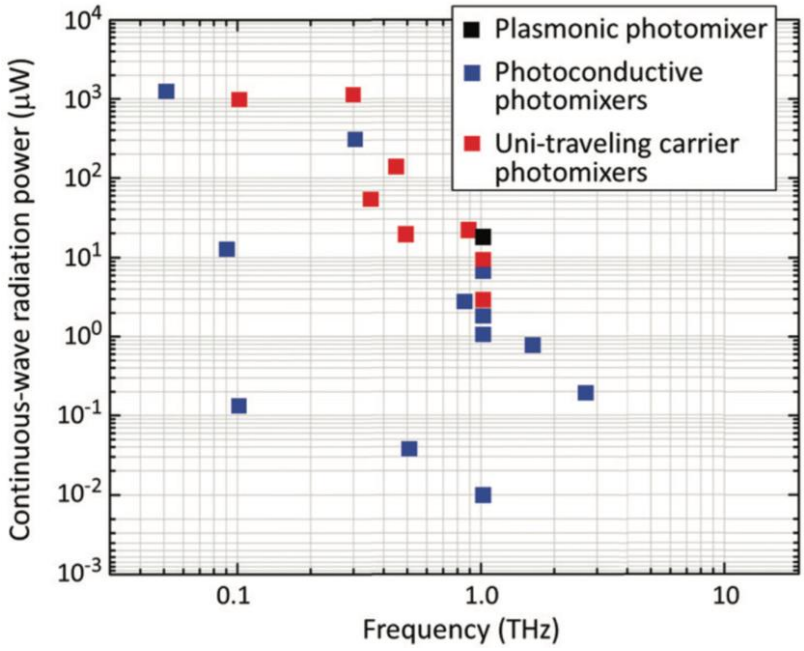

Figure 3.4 (a) The radiated power from the plasmonic photomixer at 1 THz as a function of the induced photocurrent. (b) The radiated power from the plasmonic photomixer at 1 THz and 350 mW optical pump power in comparison with previously demonstrated photomixers.

Figure 3.5(a) shows the radiated power spectrum of the LT-GaAs plasmonic photomixer over a 2 THz frequency range, which is set by tuning the frequency difference of the two pump lasers and limited by the tuning range of the pump lasers. The radiation spectrum follows the radiation characteristics of the logarithmic spiral antenna at lower frequencies and rolls off at higher frequencies due to parasitic resistance and capacitance of the photoconductor loaded to the terahertz antenna. In order to investigate the geometry dependence of the radiation power spectrum, two plasmonic photomixers are fabricated with plasmonic contact electrode areas of $10 \times 10\ \mu m^2$ and $20 \times 20\ \mu m^2$ and an end-to-end anode-cathode spacing of 10 μm. Figure 3.5(b) shows the radiation power spectra of the fabricated plasmonic photo- mixers. At lower terahertz radiation frequencies, the design with larger plasmonic contact electrode area generates higher radiation power levels compared with the design with smaller plasmonic contact electrode area. This is because the photomixer with larger plasmonic contact electrode area can be pumped by a larger pump beam size covering the device active area. Therefore, the carrier screening effect is mitigated and higher terahertz powers are achieved under the same optical pump power levels. At higher radiation frequencies, the RC roll-off starts to influence the terahertz radiation powers; thus, the design with smaller plasmonic contact electrode area starts to outperform the design with larger plasmonic contact electrode area.

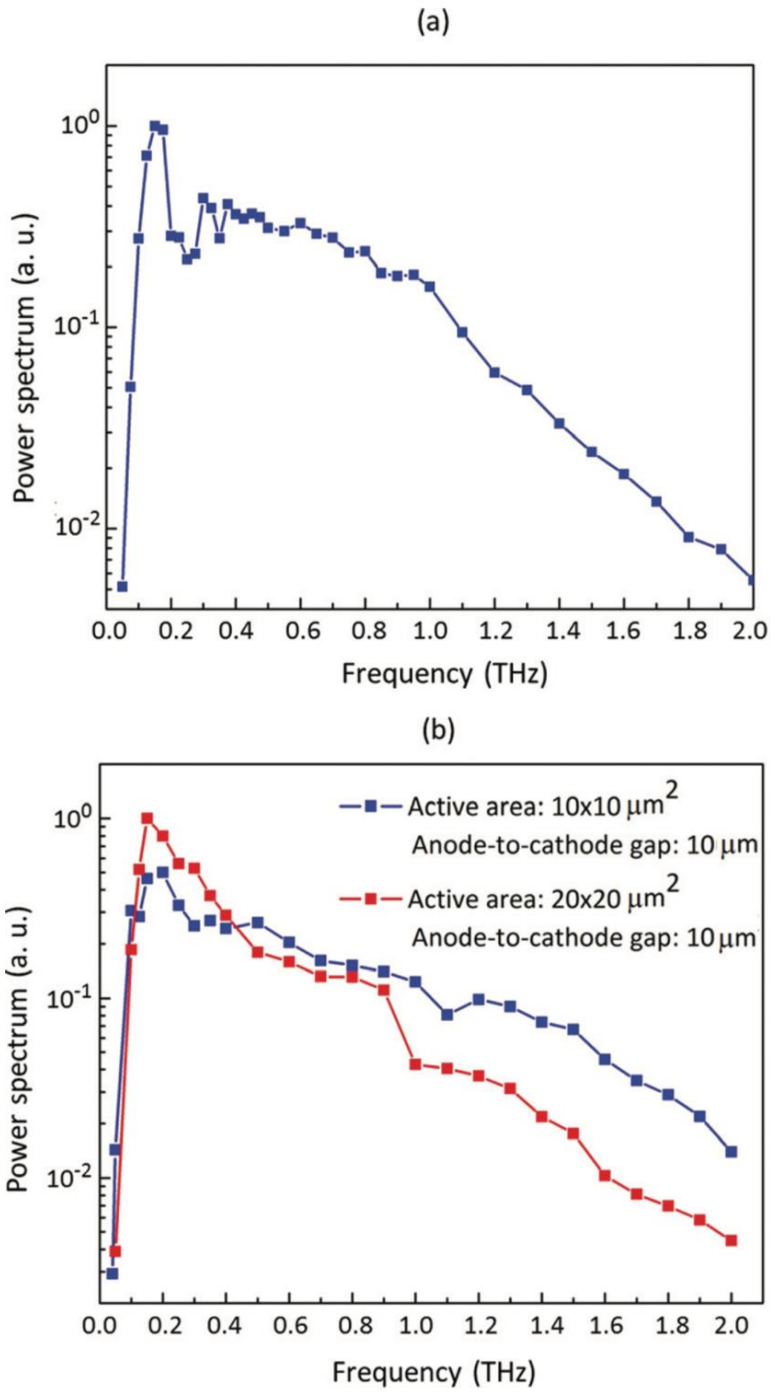

Figure 3.5 (a) Radiation spectrum of the plasmonic photomixer at an optical pump power of 350 mW and bias voltage of 20V, over a 2 THz frequency range. (b) Radiation spectrum of the plasmonic photomixers with 10 × 10 μm^2 and 20 × 20 μm^2 plasmonic contact electrode areas.

3.3 Impact of Substrate Properties on Terahertz Radiation

When the photomixer is pumped by two optical beams with a terahertz frequency difference, photo-generated carriers in the substrate are drifted to the photoconductor contact electrodes through an applied bias electric field. The induced photocurrent is fed to the terahertz antenna to generate terahertz radiation at the offset frequency of the two optical beams. Substrates with high carrier drift velocities and short carrier lifetimes are required for efficient operation of photomixers. This is because high carrier drift velocities offer high photoconductive gains, enabling high power terahertz generation. Moreover, short carrier lifetimes prevent destructive radiation from slow photocarriers [4] and the carrier screening effect [33], enabling high optical-to-terahertz conversion efficiencies. Unfortunately, most techniques used for realizing short carrier lifetime substrates introduce high defect density levels in the semiconductor lattice, which can reduce the carrier drift velocities. Therefore, in order to choose an appropriate photo-absorbing substrate for photomixers, it is very important to study the tradeoffs between the carrier drift velocity and carrier lifetime and their impact on the photomixer performance at the desired radiation frequency.

3.3.1 Short Carrier Lifetime Substrates

We investigate the impact of GaAs substrates with epitaxially embedded nanoparticles of rare-earth arsenide (RE-As) compounds, as the short carrier

lifetime photoabsorbing substrates, on the performance of plasmonic photomixers pumped at a 780 nm wavelength. By adjusting the deposition of the RE-As nanoparticles embedded inside the GaAs substrate lattice and superlattice geometry, the carrier drift velocity and carrier lifetime can be controlled [34–37]. Photomixers with plasmonic contact electrodes are used in this study due to their high quantum efficiency and high optical-to-terahertz conversion efficiency. This is because a significantly larger portion of the photocarriers is generated in close proximity to the plasmonic contact electrodes. Therefore, a larger number of photocarriers can be routed to the terahertz antenna in a sub-picosecond timescale for efficient terahertz generation and higher optical-to-terahertz conversion efficiencies can be achieved. In order to study the impact of the substrate properties on the photomixer performance, identical plasmonic photomixers are fabricated on ErAs:GaAs and LuAs:GaAs superlattice structures with different LuAs/ErAs nanoparticle depositions and superlattice geometries and their performance is compared with a plasmonic photomixer fabricated on a low temperature (LT) grown GaAs substrate [10].

ErAs:GaAs and LuAs:GaAs superlattice structures with different ErAs/LuAs nanoparticle depositions and superlattice geometries are grown by solid-source molecular beam epitaxy (MBE). Figure 3.6 shows the schematic diagram of an exemplary RE-As:GaAs superlattice structure. First, a 150-nm-thick undopedGaAs buffer layer is deposited on a semi-insulating GaAs (100) substrate

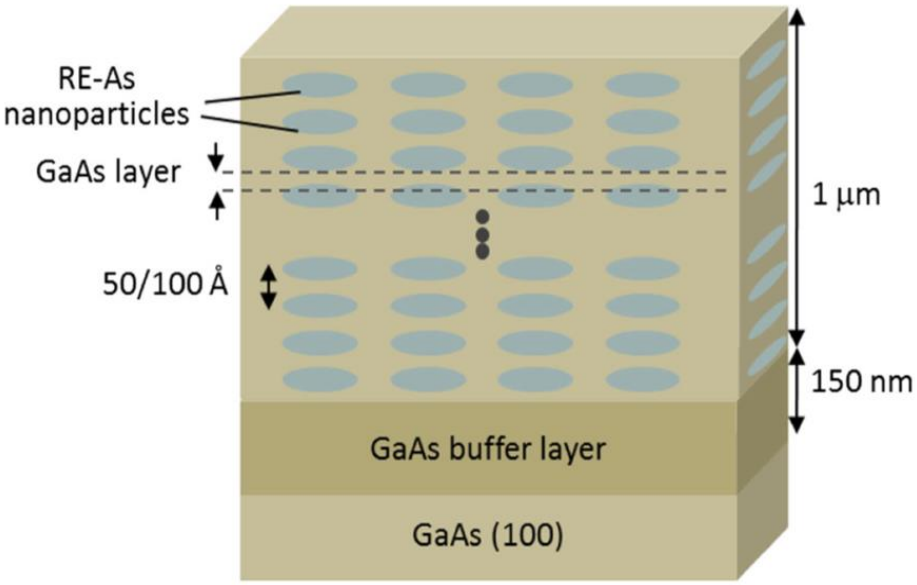

Figure 3.6 Schematic diagram of a RE-As:GaAs superlattice structures.

at 580 °C. Next, the RE-As nanoparticles are incorporated in the superlattice structure. The depositions of the RE-As nanoparticles are followed by a 50-/ 100-Å GaAs layer growth at 530 °C with an As_2/Ga beam equivalent pressure (BEP) ratio of 15 and 3×10^{-6} Torr BEP of As_2. This process is repeated 200/100 times to form a 1-µm-thick RE-As:GaAs superlattice structure. The depositions of the RE-As nanoparticles are monitored by reflection high-energy electron-diffraction (RHEED) intensity oscillations and reported in terms of an equivalent number of RE-As monolayers (ML). The superlattice thickness and periodicity are measured by high-resolution X-ray diffraction (HR-XRD). Finally, a GaAs cap layer (50/100 Å) is grown on top of the RE-As:GaAs superlattice structure for preventing oxidation of the RE-As nanoparticles. By adjusting the concentration of the RE-As nanoparticles and the geometry of the superlattice structure, the carrier mobility

Material	Carrier lifetime (ps)	Resistivity (KΩ.cm)
LT-GaAs	0.4 ps	250
ErAs:GaAs (0.15ML/50Å)×200	0.67 ps	24.5
ErAs:GaAs (0.1ML/50Å)×200	0.67 ps	12.5
LuAs:GaAs (0.5ML/100Å)×100	0.8 ps	14.7
LuAs:GaAs (0.25ML/50Å)×200	0.74 ps	3
LuAs:GaAs(0.25ML/100Å)×100	0.65 ps	12

Table 3.1 Carrier lifetime and resistivity of the LT-GaAs, ErAs:GaAs, and LuAs:GaAs substrates

and carrier lifetime is controlled. For comparison, a LT-GaAs substrate is grown on a semi-insulating GaAs (100) substrate at 250 °C with an As_2/Ga BEP ratio of 19 followed by a 10-min post-annealing process at 600 °C. The carrier lifetime values of the LT-GaAs, ErAs:GaAs, and LuAs:GaAs substrates are obtained by time-resolved differential optical pump-probe reflection measurements using femtosecond laser pulses centered at an 800 nm wavelength, with an 80 MHz repetition rate (Table 3.1). An average pump power of 10 mW, a pump and probe power ratio of 10:1, and a beam spot size of 120 μm on the sample are used for these measurements. The measured differential photo-reflectance data is fitted to an exponential curve, $I_0.exp(-t/\tau)$, where I_0 is the measured normalized differential intensity, t is the time delay of arrival between pump and probe pulses, and τ is the carrier lifetime. Additionally, the resistivity levels of the LT- GaAs, ErAs:GaAs, and LuAs:GaAs substrates are extracted from dark resistance measurements (Table 3.1).

3.3.2 Experimental Setup

Figure 3.7 shows the schematic diagram of the plasmonic photomixer fabricated on the LT-GaAs, ErAs:GaAs, and LuAs:GaAs substrates. Metallic gratings (5/45 nm Ti/Au height, 100 nm width, and 200 nm pitch) covered by a 150 nm SiO_2 anti-reflection coating are used as the plasmonic contact electrodes. This offers more than 70 % power transmissivity for a TM polarized optical pump beam at 780 nm through the plasmonic contact electrodes into the photo-absorbing substrates. Plasmonic anode and cathode contact electrodes are designed to cover a 20×20 μm^2 active area each with a 10-μm gap size between the anode and cathode contact electrodes.

This design induces a 2.2 fF capacitance between the anode and cathode contact electrodes and allows maintaining high carrier drift velocities across the entire plasmonic contact electrode area [16]. The plasmonic contact electrodes are integrated with a logarithmic spiral antenna, which offers a broadband radiation resistance of 70–100 Ω over 0.1–2 THz frequency range [38, 39]. The fabricated plasmonic photomixers are centered and mounted on a hyper hemispherical silicon lens to collect and collimate the generated terahertz radiation. Two distributed-feedback (DFB) lasers (TOPTICA #LD-0783-0080-DFB-1 and TOPTICA #LD-0785-0080-DFB-1) are used to pump the fabricated plasmonic photomixers. The offset frequency of the two DFB lasers is tuned in a 0.1–2 THz frequency range by accurately controlling their operation temperatures and driving currents. The

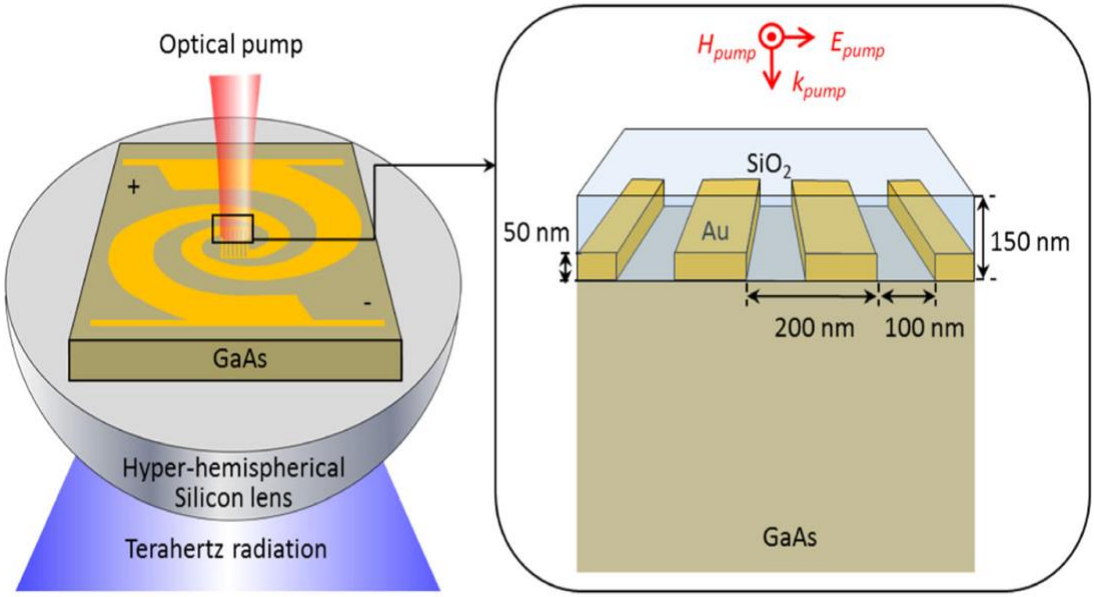

Figure 3.7 Schematic diagram of a plasmonic photomixer fabricated on the RE-As:GaAs substrate.

outputs of the two DFB lasers are coupled into a semiconductor optical amplifier (TOPTICA BOOSTA PRO 780) through a polarization-maintained fiber. An objective lens is used to asymmetrically focus the amplified optical pump onto the edge of the anode contact electrodes to maximize the induced photocurrent. The amplified optical beams from the two DFB lasers are balanced in power to achieve high optical-to-terahertz conversion efficiencies. A small portion of the amplified optical pump is simultaneously monitored on an optical spectrum analyzer by placing a pellicle between the output of the semiconductor optical amplifier and the plasmonic photomixers. Finally, the terahertz radiation from the plasmonic photomixers is collimated by a polyethylene lens and detected by a calibrated silicon bolometer from Infrared Laboratories.

3.3.3 Experimental Results

Figure 3.8(a) shows the induced photocurrent for the plasmonic photomixers fabricated on the ErAs:GaAs and LT-GaAs substrates at an optical pump power of 25 mW. The induced photocurrent is proportional to the carrier drift velocity and carrier lifetime. Therefore, assuming that the ratios between the carrier lifetimes are maintained under the 25 mW optical excitation and assuming the same carrier lifetime for electrons and holes, the measured photocurrent values indicate that higher carrier drift velocities are offered by the ErAs:GaAs (0.1ML/50 Å) × 200 substrate compared to the ErAs:GaAs (0.15ML/50 Å) × 200 substrate. This can be explained by a lower concentration of scattering centers in the ErAs:GaAs superlattice structure with lower ErAs deposition. Moreover, the LT-GaAs substrate exhibits the lowest carrier drift velocity compared to the ErAs:GaAs substrates. Figure 3.8(b) shows the radiation spectra of the plasmonic photomixers fabricated on the ErAs:GaAs and LT-GaAs substrates at an optical pump power of 25 mW and a bias voltage of 30 V. The terahertz radiation power from the fabricated photomixers at an angular frequency of ω is given by [28]:

$$P_{rad} = \frac{R_A}{2} P_{pump} \left(\frac{\eta e}{h\upsilon} \right)^2 \frac{1}{1+(\omega\tau)^2} \frac{1}{1+(\omega R_A C)^2} P_1 P_2 \tag{3.1}$$

where R_A is the terahertz antenna radiation resistance, η is the photoconductor quantum efficiency, e is the electron charge, $h\upsilon$ is the photon energy, τ is the carrier lifetime, C is the capacitive loading to the terahertz antenna, and P_1 and P_2

are the power levels of the beating optical beams that are set to be equal for maximum radiation efficiency. As expected, the plasmonic photomixer fabricated on the ErAs:GaAs (0.1ML/50 Å) × 200 substrate offers higher terahertz radiation power levels compared to the other plasmonic photomixers at low terahertz frequencies due to its higher quantum efficiency as a result of a higher carrier drift velocity. A much steeper terahertz radiation power roll-off slope is observed for the ErAs:GaAs plasmonic photomixers compared to the LT-GaAs plasmonic photomixer in the 0.3 – 1 THz frequency range. This is because the LT-GaAs plasmonic photomixer is less impacted by the destructive radiation from slow photocarriers in this frequency range due to its shorter carrier lifetime value ($\omega\tau <$ 1). The radiation power at higher frequencies ($\omega\tau >$ 1) is dominated by the RC roll-off with an estimated 3 dB roll-off frequency of ~1 THz. Since identical logarithmic spiral antennas and plasmonic contact electrode designs are used in the fabricated plasmonic photomixers, similar radiation power roll-off slopes are observed for all of the plasmonic photomixers above 1 THz. The dramatic radiation power drop at ~ 1.1 THz is due to water absorption. Despite the steeper radiation power roll-off of the ErAs:GaAs photomixers, higher terahertz power levels are offered by the ErAs:GaAs substrates compared to the LT-GaAs substrate above 1 THz. This is because the impact of the high carrier drift velocities of the ErAs:GaAs substrates on the terahertz radiation power level is more dominant than the impact of the short carrier lifetime of the LT-GaAs substrate above 1 THz (Eq. 3.1). The negative impact of the carrier screening

(a)

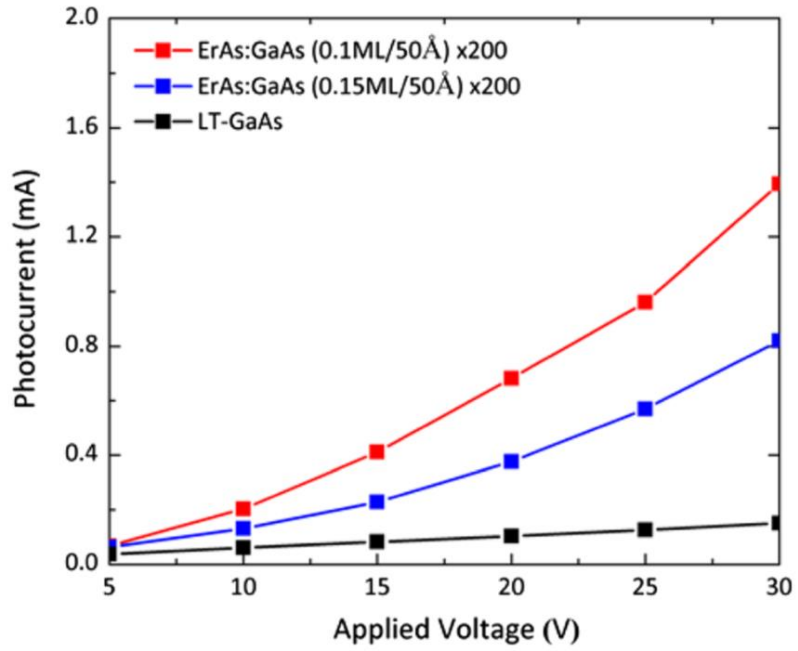

(b)

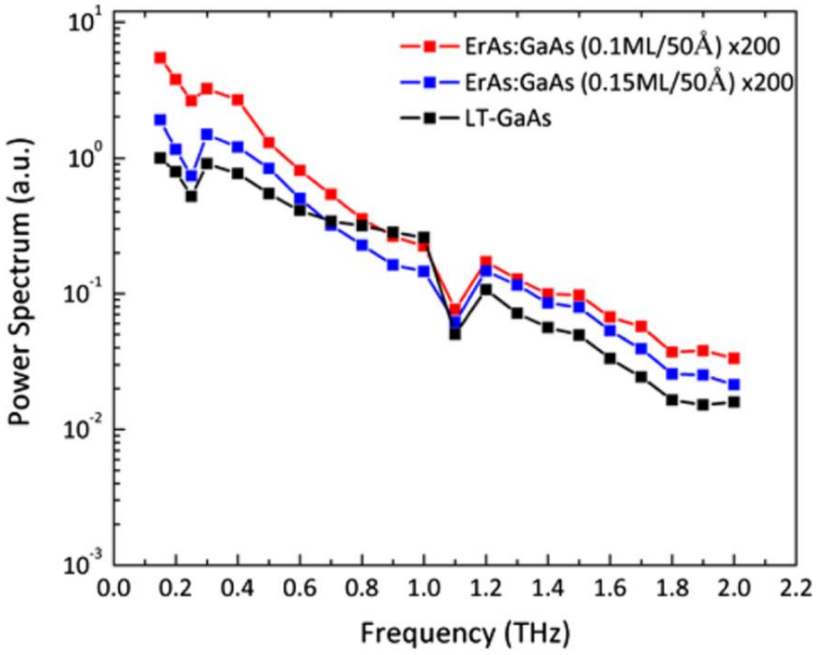

Figure 3.8 (a) The induced photocurrent for the plasmonic photomixers fabricated on the LT-GaAs and ErAs:GaAs substrates at an optical pump power of 25 mW. (b) The radiation power spectra of the plasmonic photomixers fabricated on the LT-GaAs and ErAs:GaAs substrates at an optical pump power of 25 mW and a bias voltage of 30 V over 0.1 – 2 THz frequency range.

effect on the photomixer efficiency can be observed by comparing the radiation power levels from the ErAs:GaAs (0.1ML/50 Å) × 200 and ErAs:GaAs (0.15ML/50 Å) × 200 plasmonic photomixers. Despite its superior performance in offering higher quantum efficiencies and terahertz radiation power levels at low frequencies, the ErAs:GaAs (0.1ML/50 Å) × 200 plasmonic photomixer is more severely impacted by the carrier screening effect at higher frequencies due to its higher carrier drift velocity. Therefore, it exhibits a higher level of power degradation compared to the ErAs:GaAs (0.15ML/50 Å) × 200 plasmonic photomixer. The carrier screening effect is less severe for the LT-GaAs plasmonic photomixer due to its shorter carrier lifetime.

Figure 3.9(a) shows the induced photocurrent for the plasmonic photomixers fabricated on the LuAs:GaAs and LT-GaAs substrates at an optical pump power of 25 mW. Assuming that the ratios between the carrier lifetimes are maintained under the 25 mW optical excitation and assuming the same carrier lifetime for electrons and holes, the induced photocurrent levels indicate that higher carrier drift velocities are offered by the LuAs:GaAs (0.25ML/ 100 Å) × 100 substrate compared to other LuAs:GaAs substrates. This can be explained by a lower concentration of scattering centers in the LuAs:GaAs superlattice structure with lower LuAs deposition and thicker GaAs layer. Moreover, the LT-GaAs substrate exhibits a comparable carrier drift velocity with the LuAs:GaAs (0.25ML/50 Å) × 200 substrate. It should be noted that the carrier drift velocity in LuAs:GaAs

substrates is highly affected by the quality of the GaAs overgrowth of the LuAs nanoparticles. Defects in the GaAs overgrowth are more of the point defect variety and act as both carrier scattering centers and as ultrafast recombination centers. However, their density of states is much lower than those of the LuAs nanoparticles. Therefore, these point defects will have a significant effect on the carrier drift velocity, but minimal effect on the carrier lifetime. Carrier lifetime is dominated by recombination at the LuAs nanoparticles because the point defects are bleached out at high excitation densities.

Figure 3.9(b) shows the radiation spectra of the plasmonic photomixers fabricated on the LuAs:GaAs and LT-GaAs substrates at an optical pump power of 25 mW and a bias voltage of 30 V. The plasmonic photomixer fabricated on the LuAs:GaAs (0.25ML/100 Å) × 100 substrate generates the highest terahertz radiation power at low terahertz frequencies due to its highest quantum efficiency. As expected, the plasmonic photomixers fabricated on the LT-GaAs and LuAs:GaAs (0.25ML/50 Å) × 200 substrates generate similar terahertz power levels at low terahertz frequencies due to their similar carrier drift velocities. Similar to the ErAs:GaAs plasmonic photomixers, the LuAs:GaAs plasmonic photomixers show a much steeper terahertz radiation roll-off slope compared to the LT-GaAs plasmonic photomixer in the 0.3 – 1 THz frequency range. Unlike the ErAs:GaAs plasmonic photomixers, the impact of the high carrier drift velocities of the LuAs:GaAs substrates on the terahertz radiation power levels is

(a)

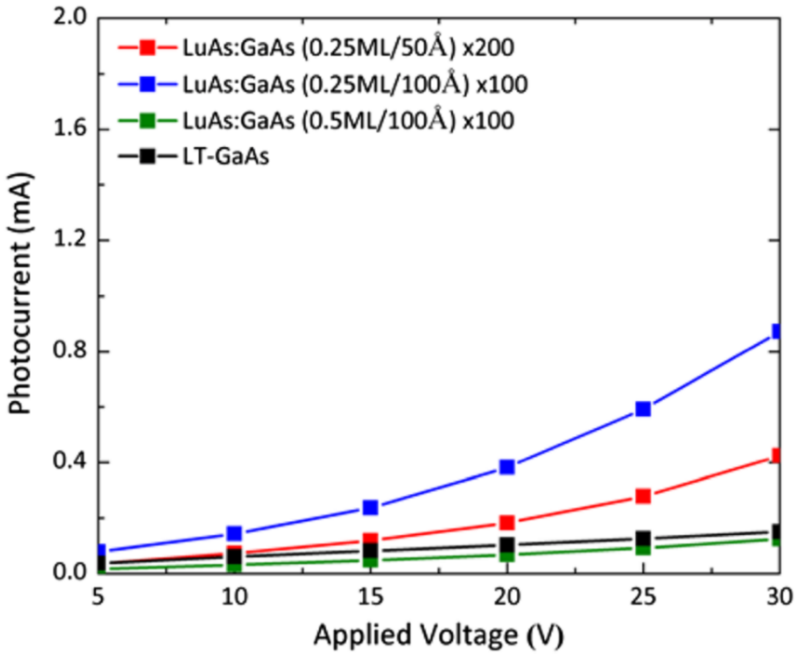

(b)

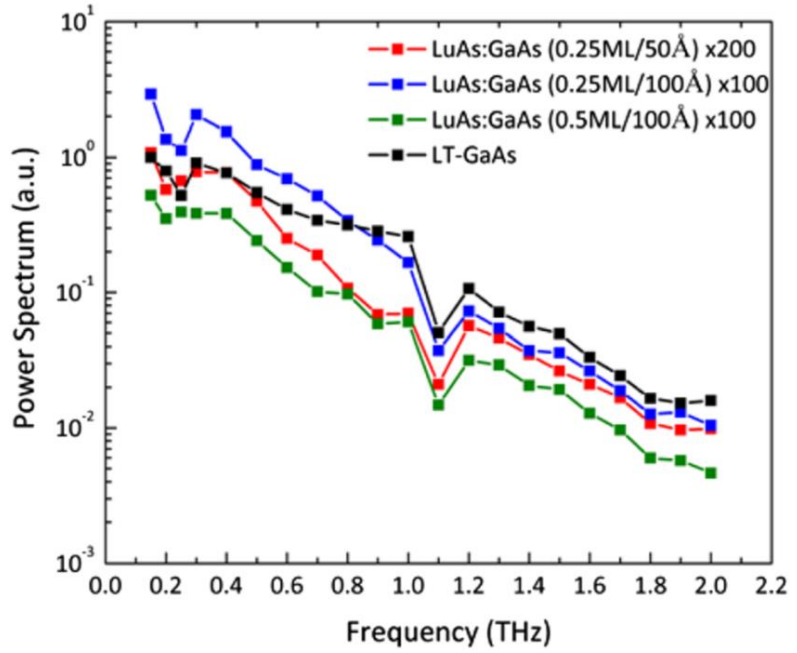

Figure 3.9 (a) The induced photocurrent for the plasmonic photomixers fabricated on the LT-GaAs and LuAs:GaAs substrates at an optical pump power of 25 mW. (b) The radiation power spectra of the plasmonic photomixers fabricated on the LT-GaAs and LuAs:GaAs substrates at an optical pump power of 25 mW and a bias voltage of 30 V over 0.1 – 2 THz frequency range.

less dominant than the impact of the short carrier lifetime of the LT-GaAs substrate above 1 THz (Eq. 3.1).

This is because of the lower carrier drift velocities of the LuAs:GaAs substrates compared to the ErAs:GaAs substrates for the ErAs/LuAs nanoparticle depositions and superlattice structures analyzed in this study. Therefore, the plasmonic photomixer fabricated on the LT-GaAs substrate generates higher terahertz radiation power levels above 1 THz compared with the plasmonic photomixers fabricated on the LuAs:GaAs substrates. Similar to the ErAs:GaAs plasmonic photomixers, the LuAs:GaAs plasmonic photomixers with higher carrier drift velocities are more severely impacted by the carrier screening effect at higher frequencies. Therefore, similar radiation power levels are offered by the LuAs:GaAs (0.25ML/ 50 Å) × 200 and LuAs:GaAs (0.25ML/100 Å) × 100 plasmonic photomixers above 1 THz. In summary, the impact of ErAs:GaAs and LuAs:GaAs superlattice structure properties on the performance of plasmonic photomixers pumped at 780 nm optical wavelength is analyzed. The results suggest that higher concentrations of scattering centers are introduced in the superlattice structures with higher ErAs/LuAs nanoparticle depositions, which lead to lower carrier drift velocities and quantum efficiencies. However, the measured carrier lifetimes do not show a significant dependence on the ErAs/LuAs nanoparticle depositions and superlattice geometries analyzed in this study. As such, ErAs:GaAs and LuAs:GaAs substrates with low ErAs/LuAs

depositions can offer higher optical-to-terahertz conversion efficiencies compared to LT-GaAs substrates. The results show that the carrier drift velocity is the most important factor that needs to be increased to achieve higher optical-to-terahertz conversion efficiencies at low terahertz frequencies. However, the carrier lifetime becomes an equally important factor that needs to be reduced to achieve higher optical-to-terahertz conversion efficiencies at higher frequencies as the terahertz radiation oscillation cycles become comparable with the carrier lifetimes. Therefore, depending on the utilized ErAs/LuAs nanoparticle depositions and superlattice geometries, ErAs:GaAs and LuAs:GaAs plasmonic photomixers could outperform LT-GaAs plasmonic photomixers at the desired terahertz radiation frequencies.

References

[1] D. Bigourd, A. Cuisset, F. Hindle, S. Matton, E. Fertein, R. Bocquet, and G. Mouret, "Detection and quantification of multiple molecular species in mainstream cigarette smoke by continuous-wave terahertz spectroscopy", *Optics Lett*er, vol. 31, pp. 2356–2358, 2006.

[2] K.J. Siebert, T. Löffler, H. Quast, M. Thomson, T. Bauer, R. Leonhardt, S. Czasch, H.G. Roskos, "All-optoelectronic continuous wave THz imaging for biomedical applications", *Physics in Medicine and Biology*, vol. 47, pp. 3743–3748, 2002.

[3] T. Kleine-Ostmann, T. Nagatsuma, "A review on terahertz communications research", *Journal of Infrared, Millimeter, and Terahertz Waves*, vol. 32, pp. 143–171, 2011.

[4] S. Preu, G. H. Dohler, S. Malzer, L. J. Wang, and A. C. Gossard, "Tunable, continuous-wave Terahertz photomixer sources and applications", *Journal of Applied Physics*, vol. 109, pp. 061301, 2011.

[5] E. R. Brown, F. W. Smith, and K. A. McIntosh, "Coherent millimeter-wave

generation by heterodyne conversion in low-temperature-grown GaAs photoconductors," *Journal of Applied Physics*, vol. 73, pp. 1480, 1993.

[6] E. Peytavit, S. Lepilliet, F. Hindle, C. Coinon, T. Akalin, G. Ducournau, G. Mouret, and J.-F. Lampin, "Milliwatt-level output power in the sub-terahertz range generated by photomixing in a GaAs photoconductor", *Applied Physics Letters*. vol. 99, pp. 223508, 2011.

[7] J. Mangeney, A. Merigault, N. Zerounian, P. Crozat, K. Blary, and J. F. Lampin, "Continuous wave terahertz generation up to 2 THz by photomixing on ion-irradiated $In_{0.53}Ga_{0.47}As$ at 1.55μm wavelengths", *Applied Physics Letters*, pp. 241102, 2007.

[8] C. W. Berry, M. R. Hashemi, S. Preu, H. Lu, A. C. Gossard, M. Jarrahi, "Plasmonics enhanced photomixing for generating quasi-continuous-wave frequency-tunable terahertz radiation", *Optics Lett*er, vol. 39, pp. 4522–4524, 2014.

[9] C. W. Berry, M. R. Hashemi, S. Preu, H. Lu, A. C. Gossard, M. Jarrahi, "High Power Terahertz Generation Using 1550 nm Plasmonic Photomixers", *Applied Physics Letters*, vol. 105, pp. 011121, 2014.

[10] S.-H. Yang, M. Jarrahi, "Frequency-Tunable Continuous-Wave Terahertz Sources based on GaAs Plasmonic Photomixers", *Applied Physics Letters*, vol. 107, pp. 131111, 2015.

[11] S.-H. Yang, R. Wans, X. Li, N. Wang, V. Cojocaru, J. O'Gorman, L. P. Barry, M. Jarrahi, "Tunable terahertz wave generation through a bimodal laser diode and plasmonic photomixer", *Optics Express*, vol. 23, pp. 31206–31215, 2015.

[12] S.-H. Yang, M. Jarrahi, "Spectral Characteristics of Terahertz Radiation from Plasmonic Photomixers", *Optics Express*, vol. 23, pp. 28522–28530, 2015.

[13] Jarrahi, "Advanced Photoconductive Terahertz Optoelectronics based on Nano-Antennas and Nano-Plasmonic Light Concentrators", *IEEE Transactions on Terahertz Science and Technology*, vol. 5, pp. 391–397, 2015.

[14] S.-H. Yang, M. R. Hashemi, C. W. Berry, M. Jarrahi, "7.5% Optical-to-Terahertz Conversion Efficiency Offered by Photoconductive Emitters with Three-Dimensional Plasmonic Contact Electrodes", *IEEE Transactions on Terahertz Science and Technology*, vol. 4, pp. 575–581, 2014.

[15] C. W. Berry, N. Wang, M. R. Hashemi, M. Unlu, M. Jarrahi, "Significant Performance Enhancement in Photoconductive Terahertz Optoelectronics by Incorporating Plasmonic Contact Electrodes", *Nature Communications*, vol. 4, pp. 1622, 2013.

[16] C. W. Berry and M. Jarrahi, "Terahertz generation using plasmonic

photoconductive gratings", *New Journal of Physics*, vol. 14, pp. 105029, 2012.

[17] S.-H. Yang and M. Jarrahi, "Enhanced light-matter interaction at nanoscale by utilizing high aspect-ratio metallic gratings", *Optics Letters*, vol. 38, pp. 3677, 2013.

[18] B.-Y. Hsieh and M. Jarrahi, "Analysis of periodic metallic nano-slits for efficient interaction of terahertz and optical waves at nano-scale dimensions", *Journal of Applied Physics*. vol. 109, pp. 084326, 2011.

[19] N. T. Yardimci, S.-H. Yang, C. W. Berry, M. Jarrahi, "High Power Terahertz Generation Using Large Area Plasmonic Photoconductive Emitters," *IEEE Transactions on Terahertz Science and Technology*, vol. 5, pp. 223–229, 2015.

[20] C. W. Berry, M. R. Hashemi, M. Jarrahi, "Generation of High Power Pulsed Terahertz Radiation using a Plasmonic Photoconductive Emitter Array with Logarithmic Spiral Antennas", *Applied Physics Letters*, vol. 104, pp. 081122, 2014.

[21] S.-G. Park, K. H. Jin, M. Yi, J. C. Ye, J. Ahn, and K.-H. Jeong, "Enhancement of terahertz pulse emission by optical nanoantenna", *ACS Nano*, vol.6, pp. 2026, 2012.

[22] E. R. Brown, "THz Generation by Photomixing in Ultrafast Photoconductors", *International Journal of High Speed Electronics and Systems.* vol. 13, pp. 497, 2003.

[23] E. Peytavit, C. Coinon, and J.-F. Lampin, "A metal-metal Fabry–Pérot cavity photoconductor for efficient GaAs terahertz photomixers", *Journal of Applied Physics*, vol. 109, pp. 016101, 2011.

[24] S. M. Duffy, S. Verhese, K. A. McIntoshy, A. Jackson, A. C. Gossard, and S. Matsuura, "Accurate Modeling of Dual Dipole and Slot Elements Used with Photomixers for Coherent Terahertz Output Power", *IEEE Transactions on Microwave Theory and Techniques*, vol. 49, pp. 1032, 2001.

[25] M. Sukhotin, E. R. Brown, A. C. Gossard, D. Driscoll, M. Hanson, P. Maker, and R. Muller, "Photomixing and photoconductor measurements on ErAs/InGaAs at 1.55 μm", *Applied Physics Letters*, vol. 82, pp. 3116, 2003.

[26] J. Bjarnason, J. Chan, A. W. M. Lee, E. R. Brown, D. C. Driscoll, M. Hanson, A. C. Gossard, and R. E. Muller, "ErAs:GaAs photomixer with two-decade tunability and 12 W peak output power", *Applied Physics Letters*, vol. 85, pp. 3983–3985, 2004.

[27] H. Ito, T. Yoshimatsu, H. Yamamoto, and T. Ishibashi, "Widely Frequency

Tunable Terahertz-Wave Emitter Integrating Uni-Traveling-Carrier Photodiode and Extended Bowtie Antenna", *Applied Physics Express*, vol. 6, pp. 064101, 2013.

[28] H. Ito, F. Nakajima, T. Furuta, K. Yoshino, Y. Hirota, and T. Ishibashi, "Photonic terahertz-wave generation using an antenna integrated uni-travelling-carrier photodiode", *Electronics Letters*, vol. 39, pp. 1828-1829, 2003.

[29] H. J. Song, K. Ajito, Y. Muramoto, A. Wakatsuki, T. Nagatsuma, and N. Kukutsu, "Uni-Travelling-Carrier Photodiode Module Generating 300 GHz Power Greater Than 1 mW", *IEEE Microwave and Wireless Components Letters*, vol. 22, pp. 363–365, 2012.

[30] F. Nakajima, T. Furuta, and H. Ito, "High-power continuous-terahertz-wave generation using resonant-antenna-integrated uni-travelling-carrier photodiode", *Electronics Letters*, vol. 40, pp. 1297–1299, 2004.

[31] E. Rouvalis, C. C. Renaud, D. G. Moodie, M. J. Robertson, and A. J. Seeds, "Traveling-wave uni-traveling carrier photodiodes for continuous wave THz generation", *Optics Express*, vol. 18, pp. 11105–11110, 2010.

[32] V. Rymanov, A. Stöhr, S. Dülme, and T. Tekin, "Triple transit region photodiodes (TTR-PDs) providing high millimeter wave output power", Optics Express, vol. 22, pp. 7550, 2014.

[33] G. C. Loata, M. D. Thomson, T. Löffler, H. G. Roskos, "Radiation field screening in photoconductive antennae studied via pulsed terahertz emission spectroscopy", *Applied Physics Letters*, vol. 91, pp. 232506, 2007.

[34] M. Griebel, J. H. Smet, D. C. Driscoll, J. Kuhl, C. A. Diez, N. Freytag, C. Kadow, A. C. Gossard, K. von Klitzing, "Tunable subpicosecond optoelectronic transduction in superlattices of self-assembled ErAs nanoislands", *Nature Material*, vol. 2, pp. 122–126, 2003.

[35] R. P. Prasankumar, A. Scopatz, D. J. Hilton, A. J. Taylor, R. D. Averitt, J. M. Zide, A. C. Gossard, "Carrier dynamics in self-assembled ErAs nanoislands embedded in GaAs measured by optical-pump terahertz-probe spectroscopy", *Applied Physics Letters*, vol. 86, pp. 201107, 2005.

[36] E. M. Krivoy, H. P. Nair, A. M. Crook, S. Rahimi, S. J. Maddox, R. Salas, D. A. Ferrer, V. D. Dasika, D. Akinwande, S. R. Bank, "Growth and characterization of LuAs films and nanostructures", *Applied Physics Letters*, vol. 101, pp. 141910, 2012.

[37] C. Kadow, S. B. Fleischer, J. P. Ibbetson, J. E. Bowers, A. C. Gossard, J. W. Dong, C. J. Palmstrom, "Self-assembled ErAs islands in GaAs: Growth and

subpicosecond carrier dynamics", *Applied Physics Letters*, vol. 75, pp. 3548-3550, 1999.

[38] Y. Huo, G. W. Taylor, and R. Bansal, "Planar Log-Periodic Antennas on Extended Hemishperical Silicon Lenses for Millimeter/Submillimeter Wave Detection Applications", *International Journal of Infrared and Millimeter Waves*, vol. 23, pp. 819–839, 2002.

[39] E. R. Brown, A. W. M. Lee, B. S. Navi, and J. E. Bjarnason, "Characterization of a planar self-complementary square-spiral antenna in the THz region", *Microwave and Optical Technology Letters*, vol. 48, pp. 524–529, 2006.

CHAPTER IV

Spectral Characterization of Plasmonic Photomixers

4.1. Overview

Recent studies have shown that incorporating plasmonic contact electrodes in photomixers can significantly enhance their quantum efficiency. By utilizing plasmonic contact electrodes, a large portion of the incident optical pump beam is localized in close proximity to the plasmonic contact electrodes and, therefore, the average transport path length of photo- generated carriers to the contact electrodes is greatly reduced [1–12]. As a result, a larger number of photocarriers reaches the plasmonic contact electrodes within a fraction of an oscillation cycle of terahertz radiation, which offers significantly higher optical-to-terahertz efficiencies compared to conventional photomixers [12–15]. While the enhanced terahertz power levels from plasmonic photomixers result in higher signal-to-noise-ratio (SNR) levels in terahertz spectroscopy and communication systems, spectral properties of the terahertz radiation from plasmonic photomixers directly impact

spectral range and resolution of terahertz spectroscopy systems as well as bandwidth of terahertz communication systems. In this chapter, we study the spectral characteristics of the terahertz radiation from plasmonic photomixers and their dependence on spectral properties of the optical pump beam.

4.2 Spectral Characterization

4.2.1 Experimental Setup

Figure 4.1 shows the experimental setup used for characterizing the spectral properties of the terahertz radiation from the plasmonic photomixer prototypes. It consists of two fiber-coupled distributed-feedback (DFB) lasers with center wavelengths of 783 nm and 785 nm and a wavelength tuning range of 2.4 nm (TOPTICA #LD-0783-0080-DFB-1 and #LD-0785-0080-DFB-1) combined in a polarization-maintaining (PM) fiber coupler and amplified by a semiconductor optical amplifier (TOPTICA BOOSTA PRO 780). The power of the two DFB lasers is balanced by accurately controlling their operating temperatures and driving currents. The amplified pump beam is collimated and asymmetrically focused onto the anode plasmonic contact electrodes of the plasmonic photomixer prototypes.

The generated terahertz radiation is coupled into a horn antenna and mixed with a terahertz local oscillator signal by use of a harmonic mixer (VDI WR2.2AMC for

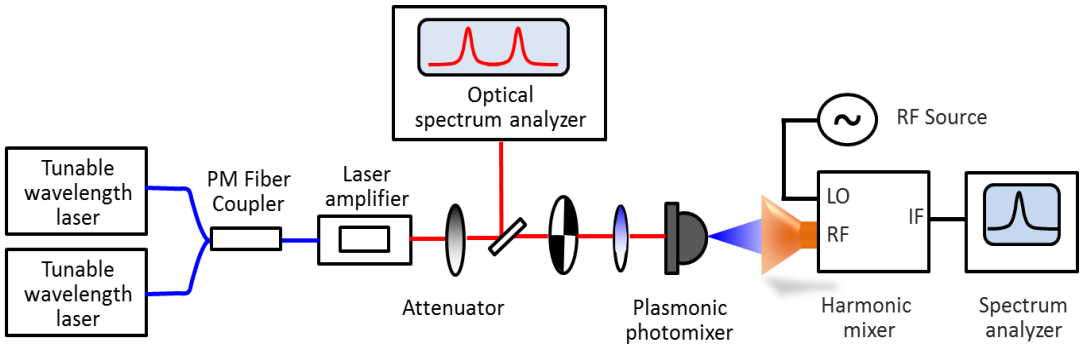

Figure 4.1 Experimental setup for characterizing the spectral properties of the terahertz radiation from the LT-GaAs plasmonic photomixer prototypes.

0.325 – 0.5 THz frequency range and VDI WR1.5AMC for 0.5 – 0.75 THz frequency range) to generate an intermediate frequency (IF) signal. The resulting IF signal, which carries the spectral characteristics of the generated terahertz radiation, is simultaneously monitored by a spectrum analyzer (HP 8566B). The frequency of the terahertz local oscillator is set to be 3 GHz off from the terahertz beating frequency of the optical pump beam to obtain an IF signal in the 3 GHz frequency range. The terahertz local oscillator is formed by a radio-frequency (RF) sweep oscillator (HP 8350B) followed by a frequency multiplier chain embedded in the harmonic mixer. A RF frequency range of 9 – 14 GHz and multiplication factors of 36 and 54 are used to generate terahertz local oscillator signals in 0.325 – 0.5 THz and 0.5 – 0.75 THz frequency ranges, respectively. It should be noted that the described spectral characterization process is limited to the 0.325 – 0.75 THz frequency range because of the frequency limitations of the harmonic mixers,

although the plasmonic photomixers can generate terahertz radiation at much higher frequencies [3].

4.2.2 Theoretical Analysis

The spectrum of the heterodyned optical pump beam and generated terahertz radiation can be calculated from the spectra of the two DFB lasers forming the optical pump beam. The spectral profiles of the two DFB lasers used in our setup, $f_{DFB1}(\omega)$ and $f_{DFB2}(\omega)$, are modeled by Gaussian functions with center frequencies of ω_{DFB1} and ω_{DFB2} and $1/e^2$ linewidths of $4\sigma_{DFB1}$ and $4\sigma_{DFB2}$, respectively.

$$f_{DFB1}(\omega) = \frac{1}{\sqrt{2\pi}\sigma_{DFB1}} e^{-\frac{(\omega-\omega_{DFB1})^2}{2\sigma_{DFB1}^2}} \tag{4.1}$$

$$f_{DFB2}(\omega) = \frac{1}{\sqrt{2\pi}\sigma_{DFB2}} e^{-\frac{(\omega-\omega_{DFB2})^2}{2\sigma_{DFB2}^2}} \tag{4.2}$$

Therefore, electric field of the heterodyned optical pump beam, which is the superposition of the electric field of the two DFB laser beams, E_{DFB1} and E_{DFB2}, is calculated as

$$E_{pump}(t) = E_{DFB1} + E_{DFB2} = E_0 \int \sqrt{f_{DFB1}(\omega)} e^{i\omega t}\, d\omega + E_0 \int \sqrt{f_{DFB2}(\omega)} e^{i\omega t}\, d\omega \tag{4.3}$$

where E_0 is the electric field of the balanced DFB lasers. As a result, the power spectrum of the heterodyned optical pump beam at the beating frequency of the two DFB lasers is calculated as

$$P_{pump}(\omega) = \frac{E_{DFB1} \otimes E_{DFB2}}{2\eta_0} = \frac{|E_0|^2}{2\eta_0} \frac{1}{\sqrt{2\pi}\sigma_{pump}} e^{-\frac{(\omega-\omega_{THz})^2}{2\sigma_{pump}^2}} \quad (4.4)$$

where η_0 is the characteristic impedance of free space and ω_{THz} is the angular beating frequency ω_{DFB1} - ω_{DFB2} set to be in the terahertz range. Therefore, the resulting heterodyned optical pump beam has a Gaussian spectrum with a $1/e^2$ linewidth of $4\sigma_{pump}$, where $\sigma_{pump} = (2\sigma_{DFB1}^2 + 2\sigma_{DFB2}^2)^{1/2}$.

When the heterodyned optical pump beam is incident on the anode plasmonic contact electrodes of the plasmonic photomixers, it generates electron-hole pairs inside the photo-absorbing substrate under the plasmonic contact electrodes. A large portion of the photo-generated electrons is drifted to the anode plasmonic contact electrodes under sufficient bias voltage levels, inducing a photocurrent that is fed to the terahertz antenna to generate terahertz radiation. The majority of the photo-generated holes are recombined inside the short-carrier lifetime semiconductor substrate before reaching the cathode contact electrodes. The frequency components of the photocurrent fed to the terahertz antenna are determined by the power spectrum of the heterodyned optical pump beam, carrier lifetime of the substrate, and geometry of the plasmonic contact electrodes. If we assume a uniform optical pump absorption under the anode plasmonic contact electrodes within absorption depth of the photo-absorbing substrate, $1/\alpha$, the density of carriers generated within the absorption depth can be calculated as [16–18]

$$\frac{dn}{dt} = \frac{\eta_e \alpha}{h\upsilon . A} P_{pump}(\omega) - \frac{n}{\tau} \tag{4.5}$$

where η_e is the photoconductor external quantum efficiency (number of generated electron- hole pairs per each incident photon), τ is the carrier lifetime of the photo-absorbing semiconductor substrate, hv is the photon energy, and A is the plasmonic contact electrode area that the optical pump beam is focused onto. Therefore, the photo-generated carrier density at the beating frequency of the two DFB lasers is calculated as

$$n(\omega) = \frac{\eta_e \alpha \tau}{h\upsilon . A} P_{pump}(\omega) \left(\frac{1}{1 + j\omega\tau} \right) \tag{4.6}$$

Since the length of the plasmonic contact electrode gratings is much shorter than terahertz wavelengths, the drifted photocurrent to various spots along the plasmonic contact electrode gratings will see an effective open circuit impedance on the open side of the gratings. Therefore, the drifted photocurrent to various spots along the plasmonic contact electrode gratings will be directly routed to the terahertz antenna connected to the plasmonic contact electrodes. Assuming a uniform optical pump distribution on the anode plasmonic contact electrode gratings, the drifted photocurrent to the terahertz antenna from the grating points that are away from the antenna by a distance l can be calculated as

$$dI(\omega) = \frac{q\eta_e \alpha \tau \mu_e}{h\upsilon . A} P_{pump}(\omega) \left(\frac{1}{1 + j\omega\tau} \right) e^{-j\omega l/V} \frac{dl}{L} \tag{4.7}$$

where q is the electron charge, μ_e is electron mobility, L is the plasmonic grating length, dl is the differential length element along the plasmonic gratings, and V is photocurrent velocity along the plasmonic contact electrode gratings. Thus, the total photocurrent fed to the terahertz antenna is calculated as

$$I(\omega) = \frac{q\eta_e \alpha \tau \mu_e}{h\upsilon . A} P_{pump}(\omega) \left(\frac{1}{1 + j\omega\tau} \right) \left(\frac{1 - e^{-j\omega L/V}}{j\omega L/V} \right) \tag{4.8}$$

If the lifetime of the carriers generated in the substrate, τ, and the maximum propagation time delay of the carriers drifted to the plasmonic contact electrodes, L/V, are much smaller than the oscillation cycle of the generated terahertz radiation ($\omega_{THz}\ \tau << 1$ and $\omega_{THz}\ L/V << 1$), the photocurrent fed to the terahertz antenna will not be affected by the carrier lifetime and plasmonic electrode geometry and will have a spectrum identical to that of the heterodyned optical pump beam. Otherwise, the intensity of the photocurrent fed to the terahertz antenna will be reduced because of the destructive interference of the photocurrents arriving at the input port of the terahertz antenna with time delays comparable with or larger than the oscillation cycle of the generated terahertz radiation. However, the spectrum of the photocurrent fed to the terahertz antenna will be identical to that of the heterodyned optical pump beam, even when the carrier lifetime and time delay along the plasmonic contact electrodes are comparable with or larger than the oscillation cycle of the generated terahertz radiation. This is because of the narrow linewidth of the heterodyned optical pump

beam relative to the pump beating frequency, resulting in almost identical level of degradation in the photocurrent intensity fed to the terahertz antenna over the entire optical pump spectral range for each terahertz beating frequency. Similarly, although radiation resistance of the terahertz antenna and device parasitics are frequency dependent, their values remain constant over the entire optical pump spectral range for each terahertz beating frequency. Therefore, the radiation power from the plasmonic photomixer prototypes, which has a quadratic dependence on the photocurrent fed to their terahertz antennas, will have a Gaussian spectrum with a $1/e^2$ linewidth of $4(\sigma_{DFB1}^{\ 2} + \sigma_{DFB2}^{\ 2})^{1/2}$. Since the linewidth of the DFB lasers (2 MHz FWHM) is much larger than that of the terahertz local oscillator (2 kHz FWHM), the measured IF spectra would be identical to the terahertz radiation spectra centered at 3 GHz with Gaussian spectral profiles and linewidths of ~2.8 MHz FWHM.

4.2.3 Experimental Results

The radiation spectra of the LT-GaAs plasmonic photomixer prototypes are characterized at an optical pump power of 150 mW and a 10 V bias voltage in the 0.34 – 0.74 THz frequency range. For this purpose, the DFB lasers are set to offer optical pump beating frequencies of 0.34, 0.42, 0.5, 0.58, 0.66, and 0.74 THz. For each optical beating frequency, the frequency of the terahertz local oscillator is set to be 3 GHz off from the optical beating frequency and the IF spectrum is measured accordingly. As an example, Fig. 4.2(a) shows the measured IF

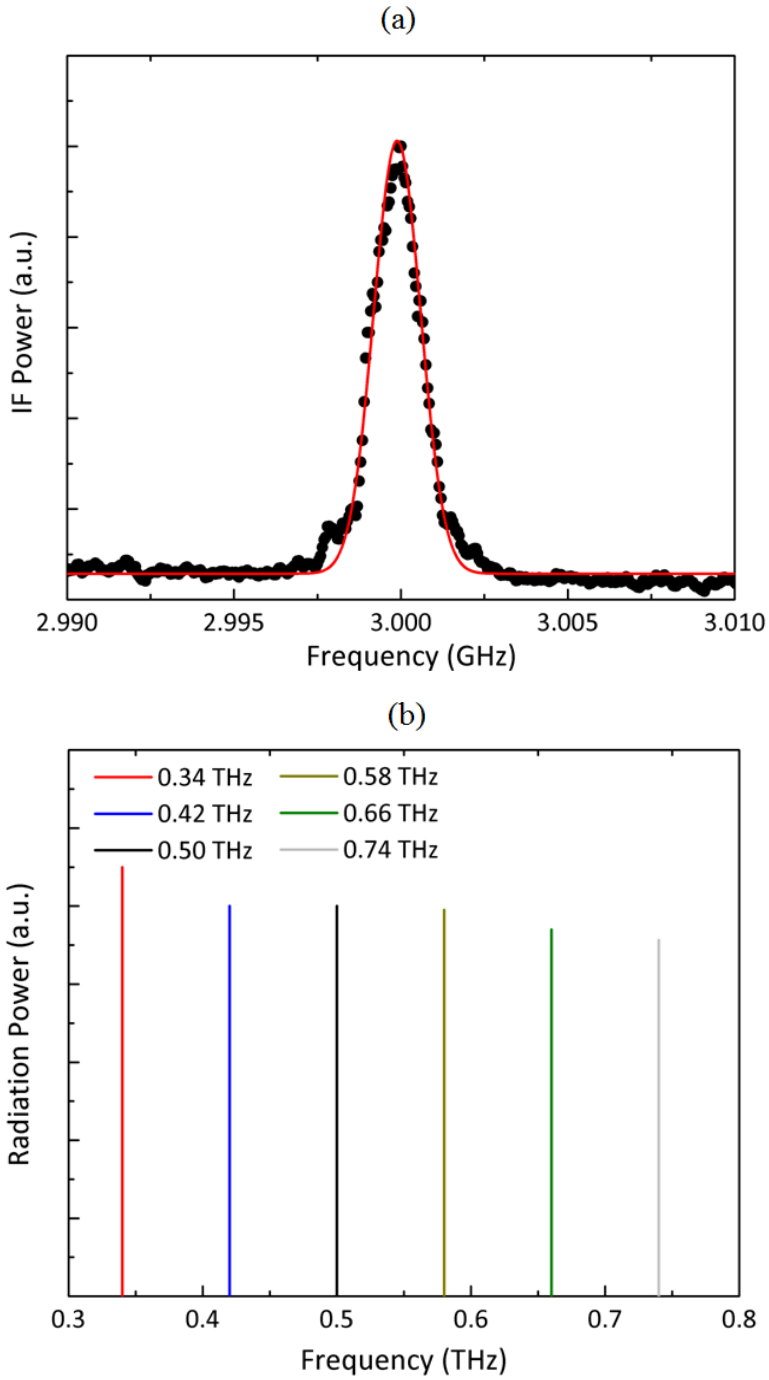

Figure 4.2 (a) The measured IF spectrum from a fabricated LT-GaAs plasmonic photomixer prototype (black dots) and the Gaussian fitting curve with a linewidth of 2.4 MHz (red line) at 0.5 THz. (b) The measured terahertz radiation spectra of the LT-GaAs plasmonic photomixer prototype at an optical pump power of 150 mW, bias voltage of 10 V, and optical pump beating frequencies in the 0.34 – 0.74 THz range.

spectrum of a plasmonic photomixer prototype at 0.5 THz. As expected, the measured spectrum has a Gaussian profile with a linewidth of 2.4 MHz FWHM.

Since the linewidth of the terahertz local oscillator is much smaller than that of the DFB lasers, the terahertz radiation spectra can be obtained by shifting each measured IF spectrum centered at 3 GHz to its corresponding optical beating frequency. Figure 4.2(b) shows the obtained terahertz radiation spectra of the plasmonic photomixer prototype. As expected, the measured IF spectra are Gaussian and maintain a spectral linewidth of ~2.8 MHz FWHM for the 0.34 – 0.74 THz frequency range. The slight terahertz power reduction at higher frequencies is mainly due to capacitive loading to the terahertz antenna, resulting in RC roll-off at higher frequencies.

Figure 4.3(a) shows the linewidth of the generated terahertz radiation as a function of frequency, exhibiting a radiation linewidth of 2 – 2.8 MHz FWHM in the 0.34 – 0.74 THz frequency range. This is in agreement with our theoretical analysis predicting the linewidth of the generated terahertz radiation to be determined by the linewidth of the two DFB lasers, which does not experience a considerable change when tuning the optical beating frequency in the 0.34 – 0.74 THz frequency range. Another way to evaluate the spectral properties of CW signal sources, which is commonly used for electronic sources, is quantifying phase noise of the output signal. Figure 4.3(b) shows the phase noise of the generated terahertz radiation, calculated from the measured spectral data, indicating that a phase noise of approximately −64 dBc/Hz at 1 MHz from the radiation center

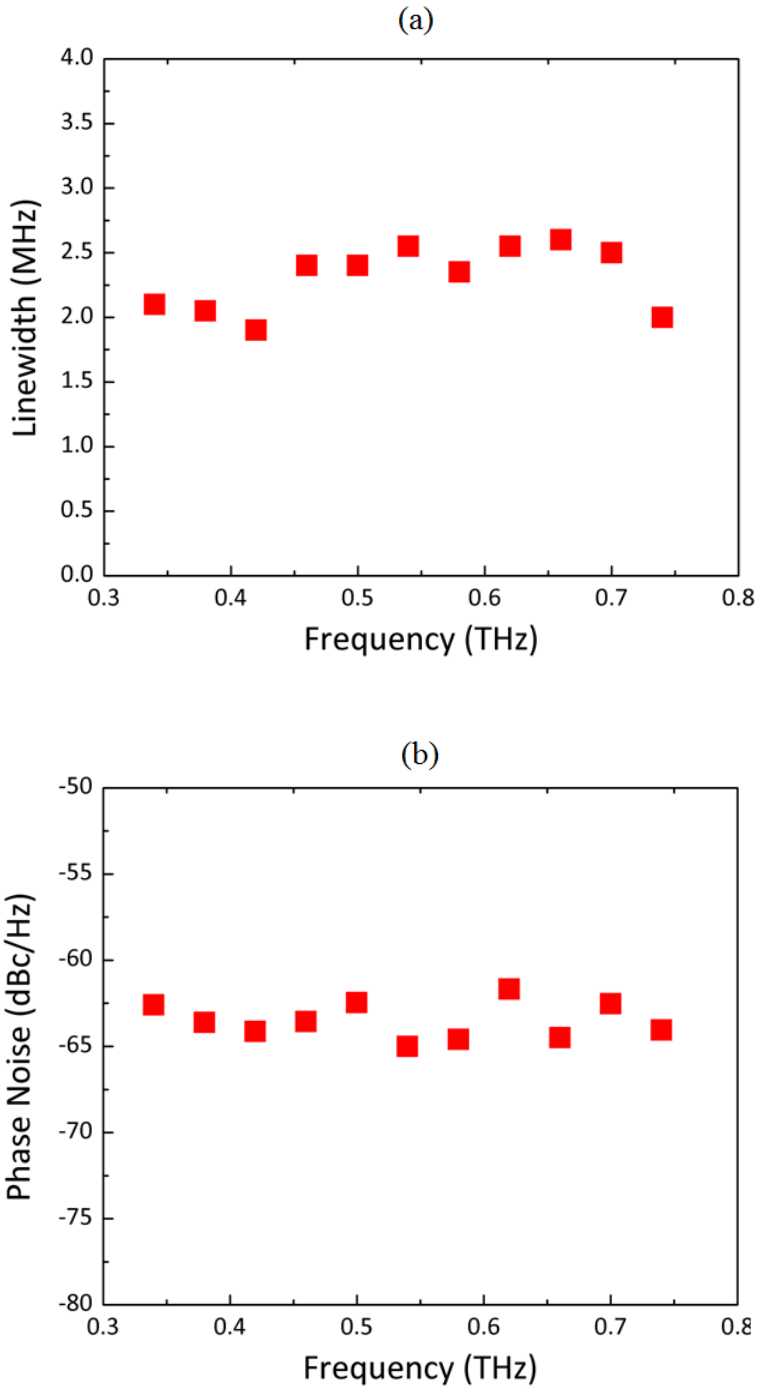

Figure 4.3 (a) The linewidth of the radiation spectra of the plasmonic photomixer prototype over the 0.34 – 0.74 THz frequency range at an optical pump power of 150 mW and bias voltage of 10 V. (b) The phase noise of the generated terahertz radiation at 1 MHz from the radiation center frequency over the 0.34–0.74THz frequency range.

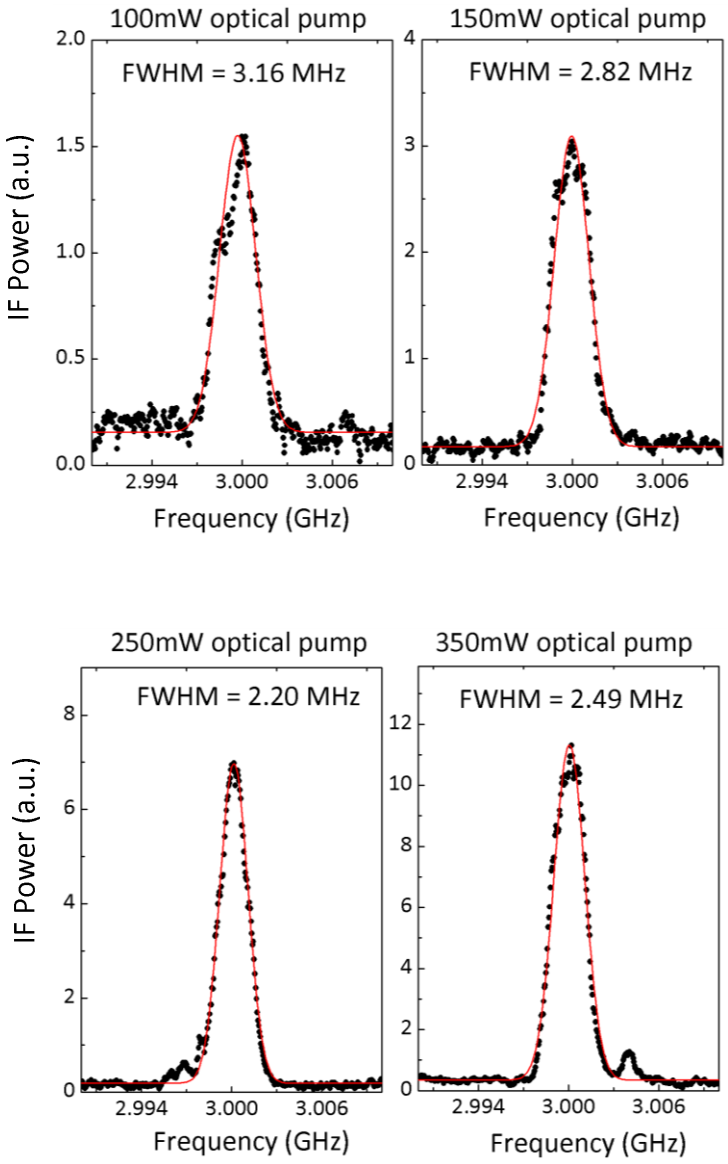

Figure 4.4 The measured IF spectra at 0.7 THz as a function of the optical pump power.

frequency is maintained over the 0.34 – 0.74 THz frequency range. The terahertz radiation spectrum of the plasmonic photomixer prototype is also characterized as a function of the optical pump power. As predicted, the same radiation linewidths are maintained in the optical pump power range of 100 – 350 mW (Fig. 4.4). This

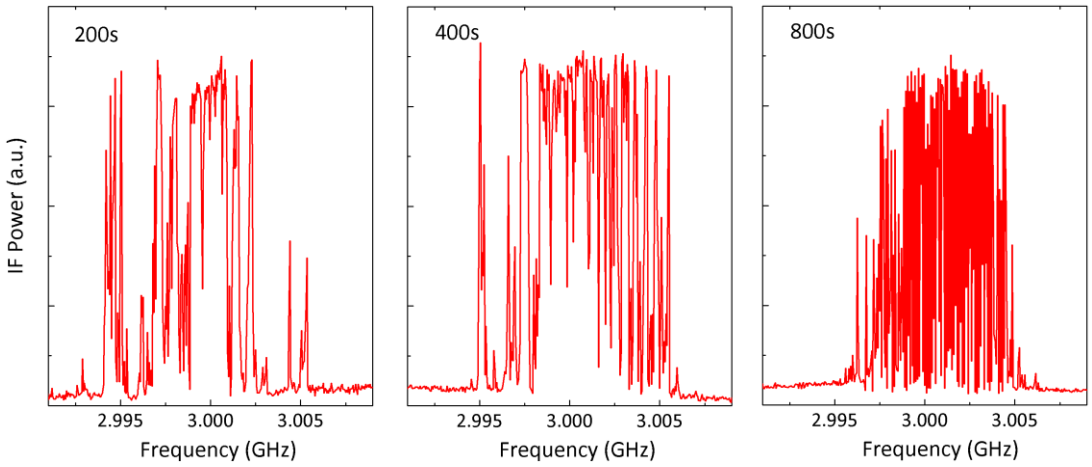

Figure 4.5 The time-integrated IF spectra at an optical beating frequency of 0.7 THz with a 200s, 400s, and 800s acquisition time.

is another indication that the terahertz radiation linewidth is only dependent on the linewidth of the optical pump beam and not the optical pump power level.

In order to investigate the impact of laser stability on the spectrum of the generated terahertz radiation, the time-integrated IF spectra are monitored during long time intervals. Figure 4.5 shows the time-integrated IF spectra at an optical beating frequency of 0.7 THz for time intervals ranging from 200 – 800 seconds. Comparing the radiation spectra at different time intervals indicates a random fluctuation in the IF center frequency with a maximum fluctuation of ~10 MHz observed over different time intervals up to 800 seconds. These observations depict the influence of the DFB laser stability characterized to be ~20 MHz RMS over 20 hours at free running condition (provided by the vendor).

References

[1] C. W. Berry, M. R. Hashemi, S. Preu, H. Lu, A. C. Gossard, M. Jarrahi,

"Plasmonics enhanced photomixing for generating quasi-continuous-wave frequency-tunable terahertz radiation", *Optics Lett*er, vol. 39, pp. 4522–4524, 2014.

[2] C. W. Berry, M. R. Hashemi, S. Preu, H. Lu, A. C. Gossard, M. Jarrahi, "High Power Terahertz Generation Using 1550 nm Plasmonic Photomixers", *Applied Physics Letters*, vol. 105, pp. 011121, 2014.

[3] S.-H. Yang, M. Jarrahi, "Frequency-Tunable Continuous-Wave Terahertz Sources based on GaAs Plasmonic Photomixers", *Applied Physics Letters*, vol. 107, pp. 131111, 2015.

[4] M. Jarrahi, "Advanced Photoconductive Terahertz Optoelectronics based on Nano-Antennas and Nano-Plasmonic Light Concentrators", *IEEE Transactions on Terahertz Science and Technology*, vol. 5, pp. 391–397, 2015.

[5] S.-H. Yang, M. R. Hashemi, C. W. Berry, M. Jarrahi, "7.5% Optical-to-Terahertz Conversion Efficiency Offered by Photoconductive Emitters with Three-Dimensional Plasmonic Contact Electrodes", *IEEE Transactions on Terahertz Science and Technology*, vol. 4, pp. 575–581, 2014.

[6] C. W. Berry, N. Wang, M. R. Hashemi, M. Unlu, M. Jarrahi, "Significant Performance Enhancement in Photoconductive Terahertz Optoelectronics by Incorporating Plasmonic Contact Electrodes", *Nature Communications*, vol. 4, pp. 1622, 2013.

[7] C. W. Berry and M. Jarrahi, "Terahertz generation using plasmonic photoconductive gratings", *New Journal of Physics*, vol. 14, pp. 105029, 2012.

[8] S.-H. Yang and M. Jarrahi, "Enhanced light-matter interaction at nanoscale by utilizing high aspect-ratio metallic gratings", *Optics Letters*, vol. 38, pp. 3677, 2013.

[9] B.-Y. Hsieh and M. Jarrahi, "Analysis of periodic metallic nano-slits for efficient interaction of terahertz and optical waves at nano-scale dimensions", *Journal of Applied Physics*. vol. 109, pp. 084326, 2011.

[10] N. T. Yardimci, S.-H. Yang, C. W. Berry, M. Jarrahi, "High Power Terahertz Generation Using Large Area Plasmonic Photoconductive Emitters," *IEEE Transactions on Terahertz Science and Technology*, vol. 5, pp. 223–229, 2015.

[11] C. W. Berry, M. R. Hashemi, M. Jarrahi, "Generation of High Power Pulsed Terahertz Radiation using a Plasmonic Photoconductive Emitter Array with Logarithmic Spiral Antennas", *Applied Physics Letters*, vol. 104, pp. 081122, 2014.

[12] S.-G. Park, K. H. Jin, M. Yi, J. C. Ye, J. Ahn, and K.-H. Jeong, "Enhancement of terahertz pulse emission by optical nanoantenna", *ACS Nano*, vol.6, pp. 2026, 2012.

[13] S. Liu, X. Shou, and A. Nahata, “Coherent detection of multiband terahertz radiation using a surface plasmon-polariton based photoconductive antenna”, *IEEE Transactions on Terahertz Science and Technology*, vol. 1, pp. 412–415, 2011.

[14] S.-G. Park, Y. Choi, Y.-J. Oh, and K.-H. Jeong, “Terahertz photoconductive antenna with metal nanoislands,” Opt. Express 20(23), 25530–25535 (2012).

[15] S.-G. Park, Y. Choi, Y.-J. Oh, and K.-H. Jeong, “Terahertz photoconductive antenna with metal nanoislands”, *Optics Express*, vol. 20, p. 25530, 2012.

[16] C. W. Berry and M. Jarrahi, “Principles of impedance matching in photoconductive antennas,” *Journal of Infrared, Millimeter and Terahertz Waves,* vol. 33, pp. 1182–1189, 2012.

[17] P. U. Jepsen, R. H. Jacobsen, and S. R. Keiding, “Generation and detection of terahertz pulses from biased semiconductor antennas,” *Journal of the Optical Society of America*, vol. 13, pp. 2424–2436, 1996.

[18] Z. Piao, M. Tani, and K. Sakai, “Carrier dynamics and terahertz radiation in photoconductive antennas,” *Japanese Journal of Applied Physics*, vol. 39, pp. 96–100, 2000.

CHAPTER V

Integrated Terahertz Sources

5.1 Dual Wavelength Optical Sources

Dual wavelength laser sources are one of the key components required for terahertz generation through photomixing [1, 2]. The wavelength tuning range and tuning speed of semiconductor lasers make them extremely suitable when frequency flexibility is required. If the outputs of two separate laser diodes are coupled together to generate the dual wavelength optical pump signal, the relative wavelength drift and uncorrelated phase noise of the two sources result in terahertz signals with poor long term stability and large phase noise. There have recently been several demonstrations of monolithic and hybrid integration of dual wavelength laser sources to increase compactness and/or correlation between the lasing modes and, thanks to this, low phase noise signal generation has been achieved [3–5]. Some of these sources employ distributed feedback (DFB) laser diode structures originally developed to emit light at fiber optic communication

wavelengths between 1300 nm and 1550 nm. One obstacle to employing these DFB structures in integrated terahertz sources has been the relative inflexibility of the technology when it is desired to incorporate DFB devices in photonic integrated circuits, especially for lower volume applications.

5.2 Bimodal Digital-DFB Laser Diode

We make use of a digital-DFB (D-DFB) technology [6, 7] to develop dual mode laser sources for terahertz generation through photomixing. The D-DFB technology uniquely enables producing low cost, high quality, single mode and dual mode laser devices by using standard InP microelectronics tool kits and processes. This allows process control of high volume InP electronics manufacturing lines to be leveraged for low cost laser production at any volume.

5.2.1 Design

Figure 5.1(a) illustrates the schematic diagram of a D-DFB laser diode. Starting with a basic Fabry–Pérot ridge waveguide laser diode, which exhibits a classic multimode Fabry–Pérot emission spectrum, features are etched into the ridge waveguide to select a single lasing mode of the Fabry–Pérot and suppress all other modes [6, 7]. This offers a new laser structure type that emits in a dynamically stable single mode spectrum [7]. Importantly, the laser does not use regrowth

technology, which results in a highly reliable device. Moreover, the digital nature of the structure etched into the upper waveguide layer allows for excellent control of both the laser emission wavelength and the stability of the chosen single mode. Another key advantage of this technology is its flexibility, allowing the realization of more complex structures such as lasers with tunable output wavelength or bimodal emission with independent tuning of the two modes [8, 9].

5.2.2 Fabrication

The two section D-DFB laser employed in this work is schematically shown in Fig. 5.1(b). The laser is a standard ridge waveguide laser diode with a ridge width of 2.5 μm. The structure is grown by low pressure metalorganic chemical vapor deposition (MOCVD) on a (100) n-type InP substrate. The laser cavity is 700 μm long and divided into two sections, section 1 and section 2 with lengths of 400 μm and 300 μm, respectively, which are separated by a 2 μm wide etched trench. The output beam is emitted from section 1. In order to achieve dual mode output wavelengths, the pattern of index perturbations in both sections is slightly different. When operated independently and around 25°C, the output wavelength from section 1 can be varied from 1536 nm to 1538.5 nm continuously, and the output wavelength from section 2 can be varied from 1536.5 nm to 1541.3 nm continuously (by varying the injection currents) [49, 52]. The ridge and index perturbations are realized in the ridge upper surface using standard etch techniques

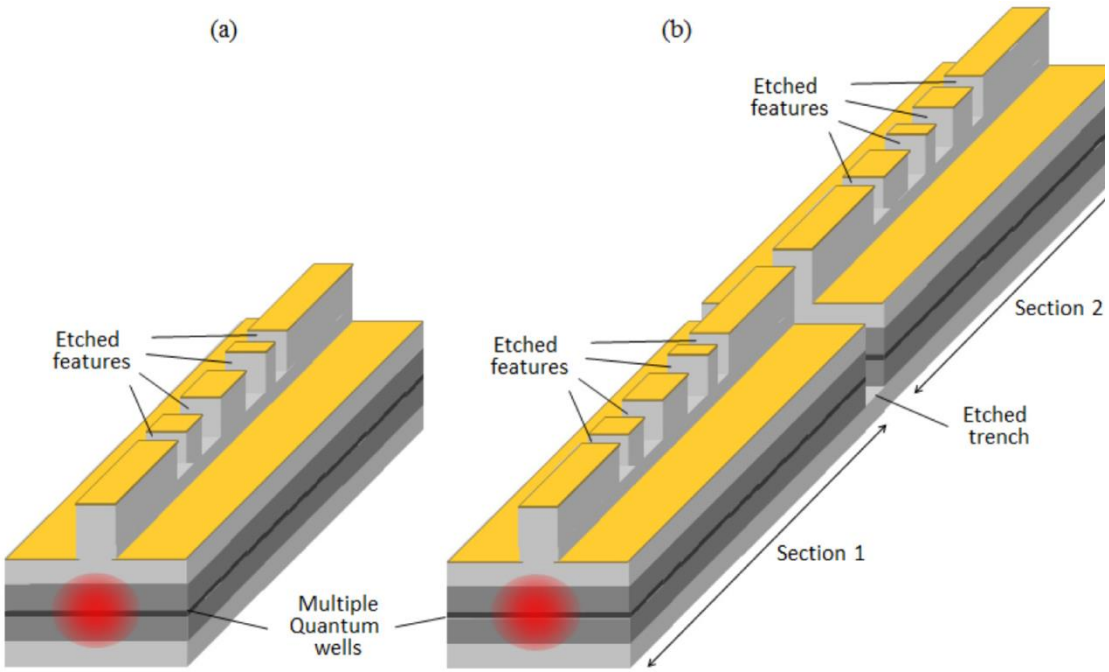

Figure 5.1 (a) The D-DFB structure showing etched features in the ridge waveguide to achieve single mode lasing. (b) Two section D-DFB structure that offers dual wavelength operation through coupling of the laser cavities.

used to fabricate Fabry–Pérot ridge waveguide lasers. SiO_2 hard masks are patterned lithographically to outline the ridge and index perturbation features. The depth of the etched features is slightly less than the height of the ridge. Dry etching using inductively coupled plasma (ICP) is used to reach approximate target depths of the features and trenches and wet etching is used to ensure uniform and accurate depths across the wafer. It should be noted that all surface etched features are in the upper wave-guiding layers and do not extend to the laser active region. The laser active region consists of five compressively strained AlGaInAs quantum wells with a well thickness of 5 nm. The final step in surface

processing is a deep ICP etching step to define the trench isolating section 1 from section 2. Since the etched trench acts as a back facet for section 1 and a front facet for section 2, a wet etching step is used to reduce the surface roughness of the trench. Electrical contacts for both sections are formed while using SiO_2 as an insulator for contact definition.

5.2.3 Operation

When both lasers are operated together, the coupling between the two laser cavities results in the generation of light at two wavelengths [10]. In the meantime, the separation between the wavelengths can be tuned by varying the temperature of the overall structure and the currents applied to the laser sections. To explain the operation in more details it should be initially considered that the laser sections have different cavity lengths and different index perturbation patterns, as outlined above. The cavity length of each section sets the Fabry–Pérot modes of that cavity. The index perturbations in each section allow the loss spectrum of the Fabry–Pérot laser to be manipulated in order to achieve single mode emission in the D-DFB structure [6, 7]. More specifically, the introduction of the index perturbations produces a loss profile with a number of loss minima spaced periodically as a function of wavelength across the gain bandwidth of the material used [8], but a given separation between the features results in just one wavelength for which the loss is minimized and lasing occurs. In the two section device employed in this

work, both laser sections have different separations between the features and different cavity lengths, resulting in loss profiles for the two sections with different periodicities [8]. The loss profile of each section can be varied by changing both the current injected into the section and the operating temperature of the device. In addition, since the lasing emission from one section is injected into the other section, and vice versa, light from one section will affect the loss profile of the other section [10]. Thus by varying the currents applied to both sections and the temperature of the device it is possible to achieve a single loss minimum for the entire device (single mode lasing) [8], or indeed two loss minima for the entire device (dual mode lasing), through application of the Vernier effect. In addition, in the single mode lasing or dual mode lasing cases, it is possible to achieve tuning of the output wavelength(s) over the entire gain bandwidth of the material (several THz) by varying the currents applied to the sections and the device operating temperature. The tuning can be continuous over small frequency ranges (several GHz) but because of the interaction between the two sections it is not possible to tune the output wavelengths independently using both sections. The typical output power of the dual wavelength source is around 0 dBm, when both sections are biased at around 50 mA. However, the output power can drop down below −5 dBm as the drive currents to the laser sections are varied to change the frequency spacing between the output wavelengths. Figure 5.2 shows the output spectrum of the two section D-DFB laser at three specific operating points (Table 5.1) that achieve spectral separations of 0.15 THz, 1.62 THz and 2.99 THz.

Frequency Separation	Temperature	Section I Injection Current	Section II Injection Current	Section I Output Wavelength	Section II Output Wavelength
0.15 THz	24.17 °C	19.25 mA	64.64 mA	1538.68 nm	1539.98 nm
1.62 THz	24.38 °C	36.65 mA	42.91 mA	1540.12 nm	1553.07 nm
2.99 THz	18.75 °C	34.19 mA	104.51 mA	1540.86 nm	1564.88 nm

Table 5.1 Operation conditions offering different spectral separations for the output of the two section D-DFB laser

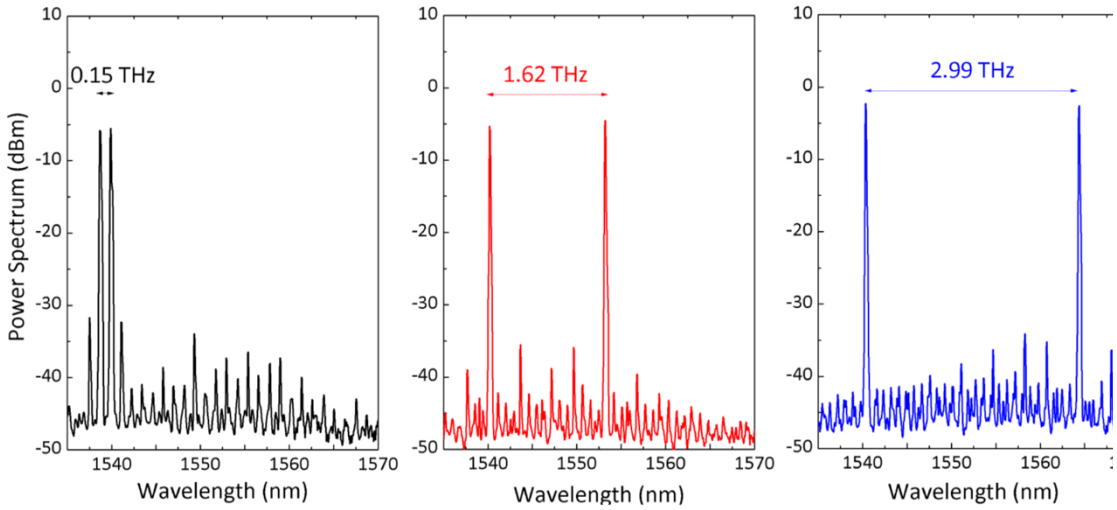

Figure 5.2 Optical spectra of the two section D-DFB laser offering two main spectral peaks in the 1550 nm wavelength range with a tunable frequency difference in 0.15-3 THz range.

It should be noted that spectral separations as low as 32 GHz are also achieved but are not presented here for figure clarity. Optical linewidth measurements for the spectral lines of the dual wavelength laser are carried out using a standard self-

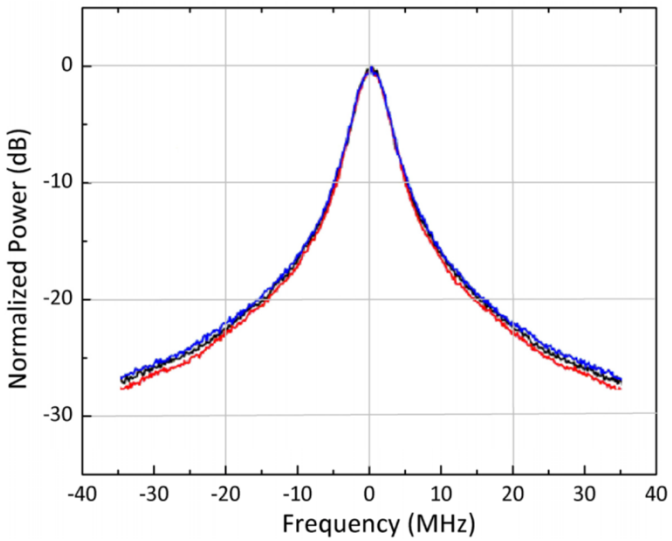

Figure 5.3 Spectral measurements for the optical lines from the implemented two section D-DFB laser at frequency separations of 1.62 THz and 0.8 THz. The black curve represents the optical line which is common to the outputs of the laser with 1.62 THz and 0.8 THz separations. The red and blue curves represent the second line from the outputs with 1.62 THz and 0.8 THz separations, respectively.

heterodyning technique [11] and linewidths of around 1 MHz are measured when the spectral separation between the lines is 1.62 THz, as shown in Fig. 5.3.

5.3 Terahertz Wave Generation

In order to achieve high optical-to-terahertz conversion efficiencies, a plasmonic photomixer is used to convert the optical beam from the two section D-DFB laser to terahertz radiation. The plasmonic photomixer is comprised of an ultrafast photoconductor with plasmonic contact electrodes integrated with a terahertz antenna on an ErAs:InGaAs substrate, as shown in Fig. 5.4(a). A logarithmic spiral antenna is used as the terahertz antenna to achieve broadband resistance of

(a) (b)

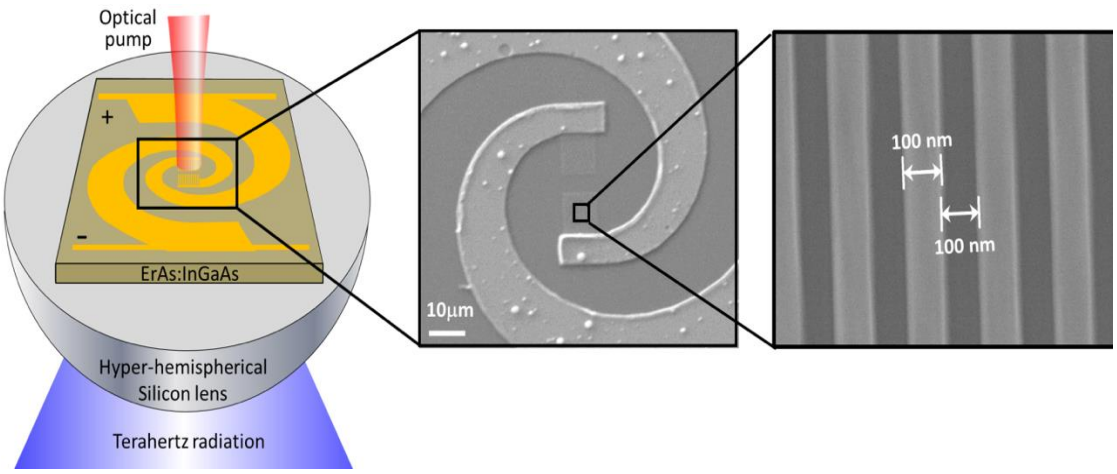

Figure 5.4 Schematic diagram and scanning electron microscope (SEM) images of the fabricated ErAs:InGaAs plasmonic photomixer with plasmonic contact electrode gratings are shown in (a) and (b) respectively.

70-100 Ω and reactance of 0 Ω over 0.15-3 THz frequency range [12, 13]. The plasmonic contact electrodes are formed by metallic gratings with 5/45 nm Ti/Au height, 100 nm width, and 200 nm pitch with a 250 nm-thick Si_3N_4 anti-reflection coating to allow transmission of more than 70% of a TM-polarized optical pump beam in the 1550 nm wavelength range through the metallic gratings into the ErAs:InGaAs substrate [14, 15]. When the optical beam from the two section D-DFB laser is incident on the anode plasmonic contact electrodes of the plasmonic photomixer, a large fraction of photo-generated carriers is generated in close proximity to the contact electrodes. This is because of excitation of surface plasmon waves along the plasmonic contact electrodes, concentrating a major portion of the incident optical beam near the plasmonic contact electrodes.

Therefore, a large number of the photo-generated electrons is drifted to the anode plasmonic contact electrodes in a sub-picosecond timescale to efficiently contribute to terahertz radiation. In the meantime, most of the photo-generated holes are recombined in the ErAs:InGaAs substrate along their drift path to the cathode contact electrode. The induced photocurrent, which has the same frequency components as the envelope of the two section D-DFB laser beam intensity, is then fed to the logarithmic spiral antenna to generate terahertz radiation at the beating frequency of the two main spectral peaks of the two section D-DFB laser.

The plasmonic photomixer is fabricated on an ErAs:InGaAs substrate with a carrier lifetime of ~0.85 ps [16]. Figure 5.4(b) shows the scanning electron microscope (SEM) images of the fabricated plasmonic photomixer. The fabrication process starts with patterning the plasmonic contact electrodes by electron-beam lithography, followed by 5/45 nm Ti/Au deposition and liftoff. The 250 nm-thick Si_3N_4 anti-reflection coating is then deposited by plasma enhanced chemical vapor deposition (PECVD). Contact vias are then formed by photolithography followed by reactive ion etching (RIE). Finally, the logarithmic spiral antenna and bias lines are formed by photolithography, followed by 10/400 nm Ti/Au deposition and liftoff. The plasmonic photomixer is centered and mounted on a hyper-hemispherical silicon lens to efficiently collect and collimate the generated terahertz radiation from the back-side of the substrate.

5.4 Experimental Setup

Figure 5.5 shows the experimental setup used for characterizing the terahertz source based on the two section D-DFB laser and ErAs:InGaAs plasmonic photomixer. The two section D- DFB laser offers two main spectral peaks in the 1550 nm wavelength range with a tunable frequency difference in the 0.15-3 THz range. The optical power level of the two main spectral peaks is balanced by controlling driving current and temperature of the two section D-DFB laser, while maintaining a side-mode suppression ratio (SMSR) of more than 25 dB. In order to prevent thermal breakdown and achieve high terahertz radiation powers at high optical pump power levels, the laser output is modulated with 2% duty cycle by an acousto-optic modulator (NEOS Technology 15200-.2-1.55-LTD-GaP-FO) and amplified by a pulsed amplifier (Optilab APEDFA-C-10). A combination of GRIN and aspheric lenses is used to focus the output optical beam onto the anode plasmonic contact electrodes of the plasmonic photomixer with a 12 μm diameter focus spot size. A quarter wave-plate followed by a linear polarizer is used to maintain a linearly polarized optical pump beam orthogonal to the plasmonic gratings. By placing a pellicle along the optical path, the spectrum of the incident optical pump beam on the plasmonic photomixer is monitored simultaneously by an optical spectrum analyzer to accurately measure the frequency of the generated terahertz radiation. Finally, the generated terahertz power is measured by a calibrated Si bolometer from Infrared Laboratories.

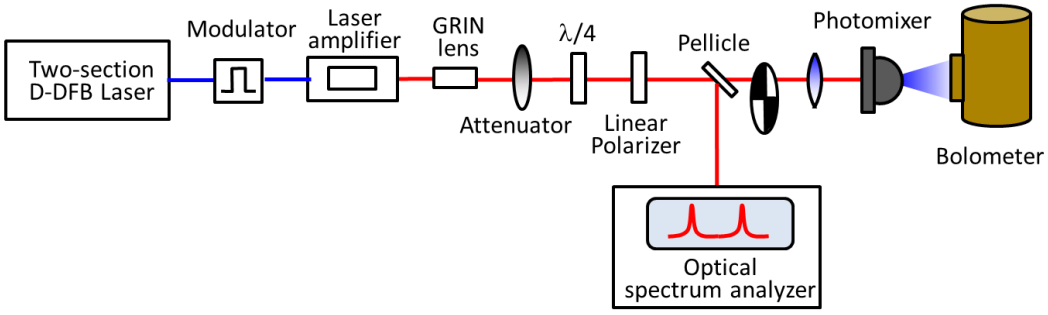

Figure 5.5 Experimental setup for characterizing the terahertz source based on the two section D- DFB laser and plasmonic photomixer.

5.5 Experimental Results

Figure 5.6(a) shows the induced photomixer photocurrent as a function of the average optical pump power and bias voltage, indicating a linear dependence on the optical pump power and bias voltage within 20-100 mW and 0-4 V ranges. Figure 5.6(b) shows the measured terahertz radiation power as a function of the induced photocurrent at each CW radiation cycle for different optical pump powers and radiation frequencies, indicating a quadratic relation between the radiated power and the induced photocurrent at each radiation frequency. As illustrated in Fig. 5.7(a), the radiation power drops at higher frequencies due to photomixer parasitics, resulting in a RC roll-off in device frequency response. At an average optical pump power of 100 mW and a bias voltage of 4 V, terahertz radiation powers as high as 1.3 mW, 106 μW, and 12 μW are achieved at each CW

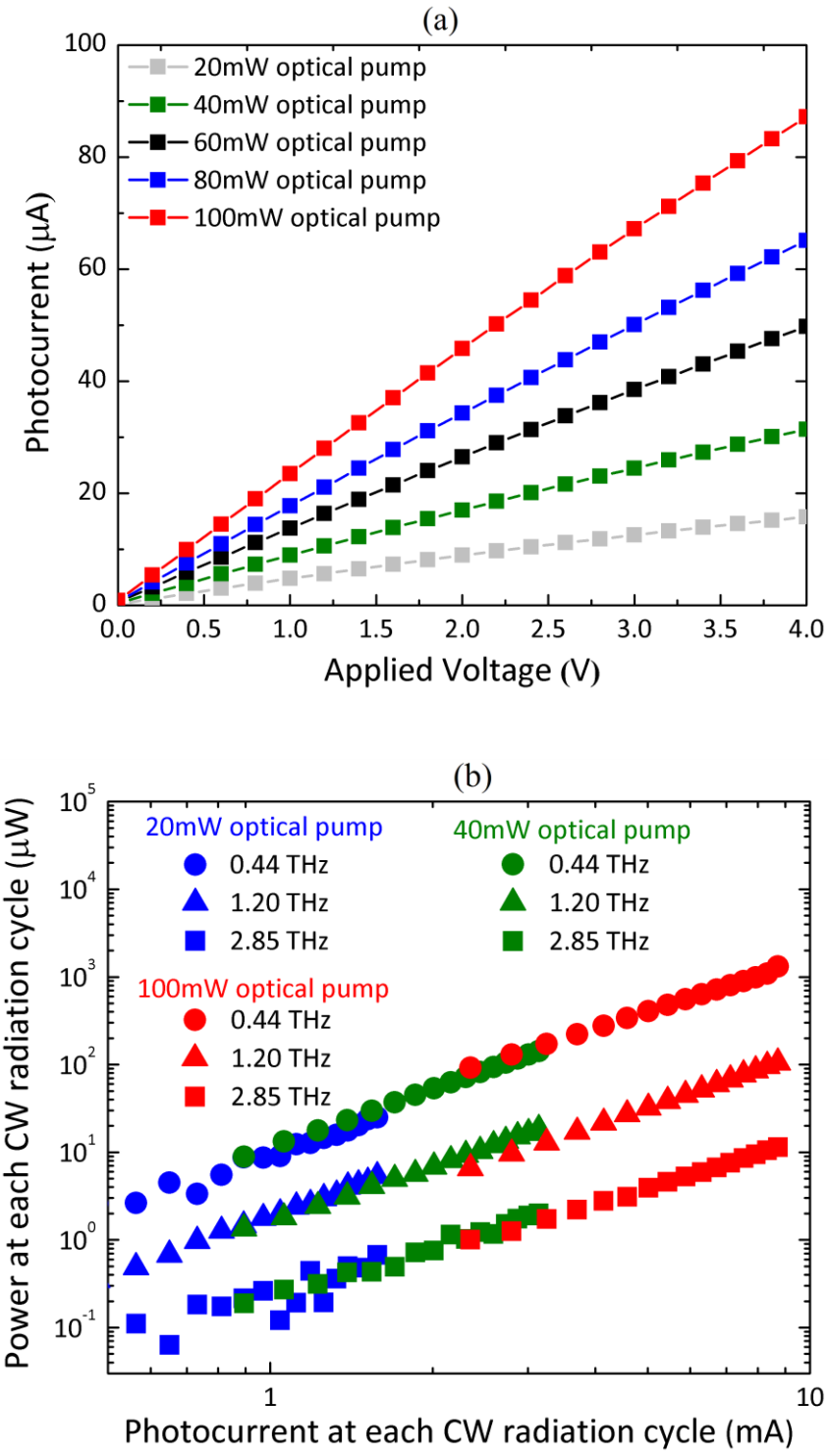

Figure 5.6 (a) The induced photomixer photocurrent as a function of the average optical pump power and bias voltage. (b) The radiated terahertz power as a function of the induced photocurrent at each CW radiation cycle at different optical pump powers and radiation frequencies.

(a)

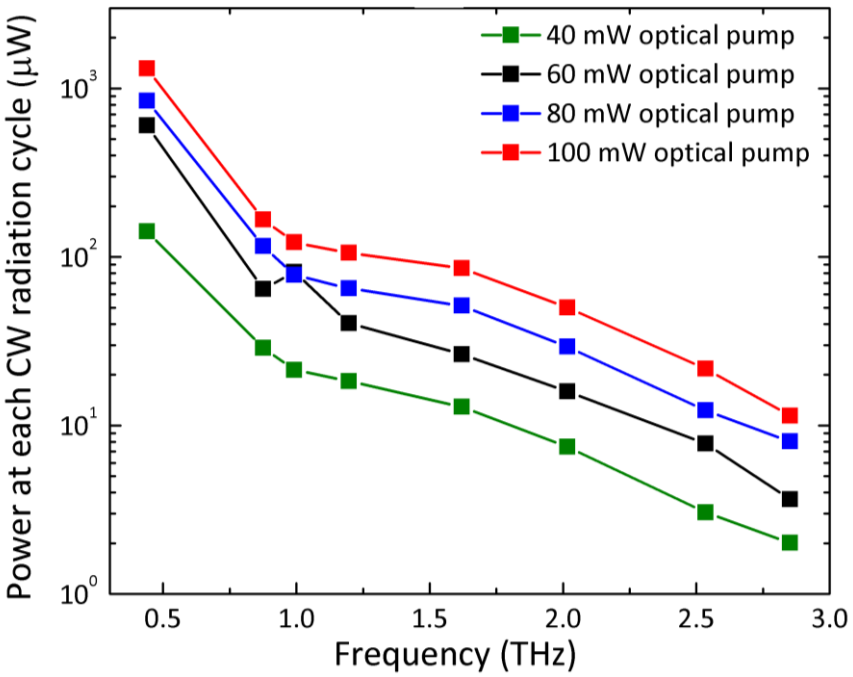

(b)

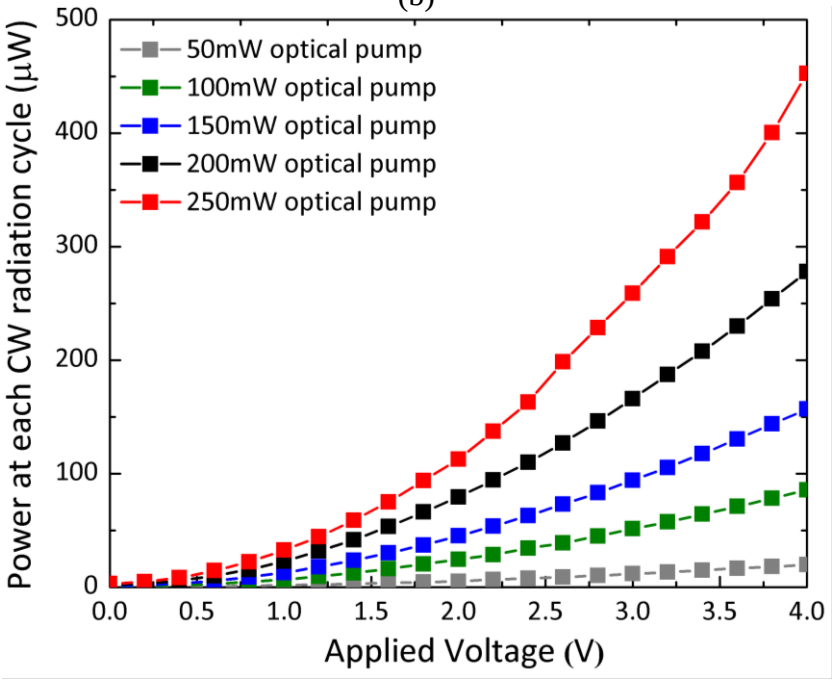

Figure 5.7 (a) The radiated terahertz power at each CW radiation cycle as a function of the average optical pump power over a 3 THz range. (b) The radiated terahertz power at each CW radiation cycle as a function of the average optical pump power and bias voltage at 1.62 THz.

radiation cycle at 0.44 THz, 1.20 THz, and 2.85 THz, respectively. Higher terahertz radiation powers are achieved at higher optical pump powers. Figure 5.7(b) shows the measured radiation power at each CW radiation cycle at 1.62 THz as a function of the average optical pump power and bias voltage. Radiation powers as high as 450 μW are achieved at 1.62 THz at an average optical pump power of 250 mW. Linewidth measurements for the generated signal are carried out at 150 GHz by using an electrical spectrum analyzer incorporating a harmonic GaAs diode mixer [17]. The results demonstrate radiation linewidths of ~2 MHz, which are expected for the employed dual wavelength laser with optical linewidths of ~1 MHz. As the process for terahertz signal generation is the same at higher frequencies, the linewidth of the generated signal will remain in the 2 MHz range at higher terahertz frequencies. In the meantime, external phase locking of the dual wavelength signals could be employed for applications that require lower phase noise levels [18]. Stability measurements for the generated signal are also performed at 150 GHz, exhibiting a frequency stability of less than 5 MHz over a 1 minute time frame.

References

[1] M. Wichmann, M. Stein, A. Rahimi-Iman, S. W. Koch, and M. Koch, "Interferometric characterization of a semiconductor disk laser driven terahertz source", *Journal of Infrared, Millimeter, and Terahertz Waves*, vol. 35, pp. 503–508, 2014.

[2] N. Kim, S.-P. Han, H. Ko, Y. A. Leem, H.-C. Ryu, C. W. Lee, D. Lee, M. Y. Jeon,

S. K. Noh, and K. H. Park, "Tunable continuous-wave terahertz generation/detection with compact 1.55 μm detuned dual-mode laser diode and InGaAs based photomixer", *Optics Express*, vol. 19, pp. 15397–15403, 2011.

[3] R. J. Steed, L. Ponnampalam, M. J. Fice, C. C. Renaud, D. C. Rogers, D. G. Moodie, G. D. Maxwell, I. F. Lealman, M. J. Robertson, L. Pavlovic, L. Naglic, M. Vidmar, and A. J. Seeds, "Hybrid integrated optical phase-lock loops for photonic terahertz sources", *IEEE Journal of Selected Topics in Quantum Electronics*, vol. 17, pp. 210–217, 2011.

[4] A. R. Criado, P. Acedo, G. Carpintero, C. de Dios, and K. Yvind, "Observation of phase noise reduction in photonically synthesized sub-THz signals using a passively mode-locked laser diode and highly selective optical filtering," Optics Express, vol. 20, pp. 1253–1260, 2012.

[5] F. van Dijk, G. Kervella, M. Lamponi, M. Chtioui, F. Lelarge, E. Vinet, Y. Robert, M. J. Fice, C. C. Renaud, A. Jimenez, and G. Carpintero, "Integrated InP heterodyne millimeter wave transmitter", *IEEE Photonics Technology Letters*, vol. 26, pp. 965–968, 2014.

[6] J. Patchell, D. Jones, B. Kelly, and J. O'Gorman, "Specifying the wavelength and temperature tuning range of a Fabry–Perot laser containing refractive index perturbations", *Proceeding SPIE*, vol. 5825, vol. 11, 2005.

[7] B. Corbett and D. McDonald, "Single longitudinal mode ridge waveguide 1.3 μm Fabry-Perot laser by modal perturbation", *Electronics Letters,* vol. 31, pp. 2181–2182, 1995.

[8] R. Phelan, W.-H. Guo, Q. Lu, D. Byrne, B. Roycroft, P. Lambkin, B. Corbett, F. Smyth, L. P. Barry, B. Kelly, J. O'Gorman, and J. F. Donegan, "A novel two-section tunable discrete mode Fabry-Perot laser exhibiting nanosecond wavelength switching", *IEEE Journal of Quantum Electronics*, vol. 44, pp. 331–337, 2008.

[9] S. Osborne, S. O'Brien, K. Buckley, R. Fehse, A. Amann, J. Patchell, B. Kelly, D. R. Jones, J. O'Gorman, and E. P. O'Reilly, "Design of single-mode and two-color Fabry–Pérot lasers with patterned refractive index", *IEEE Journal of Selected Topics in Quantum Electronics*, vol. 13, pp. 1157–1163, 2007.

[10] J. Hong, R. Finlay, R. Tong, C. Rogers, and D. Goodchild, "Simultaneous dual-wavelength operationin cascaded strongly gain-coupled DFB lasers", *IEEE Photonics Technology Letters*, vol. 11, pp. 1354–1356, 1999.

[11] T. Okoshi, K. Kikuchi, and A. Nakayama, "Novel method for high resolution measurement of laser output spectrum", *Electronics Letters*, vol, 16, pp. 630–631,

1980.

[12] Y. Huo, G. W. Taylor, and R. Bansal, “Planar log-periodic antennas on extended hemishperical silicon lenses for millimeter/submillimeter wave detection applications”, *Journal of Infrared, Millimeter and Terahertz Waves*, vol. 23, pp. 819–839, 2002.

[13] C. W. Berry, M. R. Hashemi, M. Jarrahi, “Generation of High Power Pulsed Terahertz Radiation using a Plasmonic Photoconductive Emitter Array with Logarithmic Spiral Antennas”, *Applied Physics Letters,* vol. 104, pp. 081122, 2014.

[14] C. W. Berry, M. R. Hashemi, S. Preu, H. Lu, A. C. Gossard, M. Jarrahi, “Plasmonics enhanced photomixing for generating quasi-continuous-wave frequency-tunable terahertz radiation”, *Optics Lett*er, vol. 39, pp. 4522–4524, 2014.

[15] C. W. Berry, M. R. Hashemi, S. Preu, H. Lu, A. C. Gossard, M. Jarrahi, “High Power Terahertz Generation Using 1550 nm Plasmonic Photomixers”, *Applied Physics Letters,* vol. 105, pp. 011121, 2014.

[16] C. Kadow, S. B. Fleischer, J. P. Ibbetson, J. E. Bowers, A. C. Gossard, J. W. Dong, and C. J. Palmstrom, “Self-assembled ErAs islands in GaAs: growth and subpicosecond carrier dynamics”, *Applied Physics Letters*, vol. 75, pp. 3548– 3550, 1999.

[17] E. Rouvalis, C. C. Renaud, D. G. Moodie, M. J. Robertson, and A. J. Seeds, “Continuous wave terahertz generation from ultra-fast InP based photodiodes”, *IEEE Transactions on Microwave Theory and Techniques*, vol. 60, pp. 509–517, 2012.

[18] A. Rolland, G. Loas, M. Brunel, L. Frein, M. Vallet, and M. Alouini, “Non-linear optoelectronic phase-locked loop for stabilization of opto-millimeter waves: towards a narrow linewidth tunable THz source”, *Optics Express*, vol. 19, pp. 17944–17950, 2011.

CHAPTER VI

Conclusion

In summary, we present the design rules, theoretical analysis, and experimental characterization of high-performance continuous-wave and broadband photoconductive terahertz sources based on plasmonic contact electrodes on a variety of short carrier lifetime substrates. With the use of plasmonic contact electrodes, we can manipulate the spatial distribution of photocarriers in the substrate and concentrate the majority of the photocarriers in close proximity to the contact electrodes. This way, the majority of the photocarriers can reach the contact electrode in a fraction of a terahertz oscillation cycle. Therefore, high quantum efficiencies and high optical-to-terahertz conversion efficiencies can be achieved. By utilizing three-dimensional plasmonic contact electrodes, we experimentally demonstrate a record-high optical-to-terahertz conversion efficiency of 7.5%, exhibiting three orders of higher optical-to-terahertz conversion efficiency compared to conventional photoconductive terahertz source designs.

We also demonstrate a LT-GaAs plasmonic photomixer based on 2D plasmonic contact electrodes, which offers a 3-fold higher radiation power level at 1 THz compared to the state-of-the-art broadly tunable CW terahertz sources. The phase noise and spectral linewidth of the generated terahertz radiation from the demonstrated plasmonic photomixer are directly determined by the spectral properties of the optical pump beam. Therefore, the spectral properties of the generated terahertz radiation remain unchanged at different radiation frequencies and power levels. This shows the ultimate importance of the spectral characteristics of optical pump sources in developing high-performance CW terahertz radiation sources for high spectral resolution, high accuracy, broadband terahertz spectroscopy systems and high-data-rate wireless communication systems.

Finally, we present a high-performance terahertz source composed of a novel two-section digital distributed feedback laser diode and a plasmonic photomixer. The presented terahertz source offers more than 3 THz radiation frequency tuning range and generates mW-level radiation power levels as high at 1.62 THz through a compact device platform, making it attractive for portable terahertz imaging, terahertz sensing, and ultra-high-data-rate wireless communication systems.